Editors' Suggestion

Topological correspondence between magnetic space group representations and subdimensions

Adrien Bouhon,[1,2,*] Gunnar F. Lange,[3] and Robert-Jan Slager[3,†]

[1]*Nordic Institute for Theoretical Physics (NORDITA), NORDITA, Hannes Alfvéns väg 12, 106 91 Stockholm, Sweden*

[2]*Department of Physics and Astronomy, Uppsala University, Box 516, SE-751 21 Uppsala, Sweden*

[3]*TCM Group, Cavendish Laboratory, University of Cambridge, J.J. Thomson Avenue, Cambridge CB3 0HE, United Kingdom*

(Received 23 November 2020; accepted 1 June 2021; published 16 June 2021)

The past years have seen rapid progress in the classification of topological materials. These diagnostical methods are increasingly getting explored in the pertinent context of magnetic structures. We report on a general class of electronic configurations within a set of antiferromagnetic-compatible space groups that are necessarily topological. Interestingly, we find a systematic correspondence between these antiferromagnetic phases to necessarily nontrivial topological ferro/ferrimagnetic counterparts that are readily obtained through physically motivated perturbations. Addressing the exhaustive list of magnetic space groups in which this mechanism occurs, we also verify its presence on planes in 3D systems that were deemed trivial in existing classification schemes. This leads to the formulation of the concept of *subdimensional topologies*, featuring nontriviality within part of the system that coexists with stable Weyl points away from these planes, thereby uncovering novel topological materials in the full 3D sense that have readily observable features in their bulk and surface spectrum.

DOI: 10.1103/PhysRevB.103.245127

I. INTRODUCTION

With the advent of topological insulators (TIs)—gapped quantum matter having a topological entity by virtue of symmetry—the past years have seen a reinvigorated interest in band theory. Time reversal symmetry (TRS) has played a major role in these developments, standing at the basis of the developments of the first models of the general notion of symmetry protected states [1,2]. More recently, the interplay with crystalline symmetries has provided a plethora of topological characterizations [3–22]. In particular, it was found that a substantial fraction of topological materials can be diagnosed by refined symmetry eigenvalue methods. Heuristically this pertains to considering combinatorial constraints between high-symmetry momenta in the Brillouin zone (BZ), which can be shown to reveal classes of band structures that actually match the full machinery of K-theory analysis in certain cases [23], and then comparing them to real space atomic limits in order to define nontriviality with respect to this reference [24,25].

Despite the crucial role of TRS, arguably the most paradigmatic TI model actually involves the formulation of TRS-breaking Chern bands [26], manifesting the original inspiration of these pursuits by quantum Hall effects. Hence, it is of natural interest to consider the role of magnetism in combination with the above recent developments. While the interplay of topology and magnetism entails a vast and established literature, ranging from spin liquids to axion insulators [27–33], there have been rather fruitful results on both essential symmetry eigenvalues indicated schemes [34], that is symmetry indicators [35] and, very recently, topological quantum chemistry [36].

Already in the nonmagnetic case the refined evaluations resulted in new insights. In particular, the discrepancies between different approaches culminated in the formulation of the concept of fragile topology [37]. These are topological invariants that, unlike stable counterparts, characterize band subspaces separated by energy gaps from the other bands that can be trivialized upon the closing of the gaps [38–41]. Of particular interest are systems with PT or C_2T symmetry that were early characterized through a stable $\mathbf{Z}_2$ invariant [42–45], and more recently through a fragile $\mathbf{Z}$ invariant [38,46] given by the Euler class [47–49] for which new physical effects have been predicted [50]. In fact, taking into account multiple gap conditions [49], these phases go beyond any symmetry eigenvalue indicated notion and relate to the momentum space braid trajectories of non-Abelian frame-charge characterized spectral nodes [48,51,52]. The role of C_2T symmetry has also been pointed out in the nontrivial topology of the low energy bands of twisted bilayer graphene [53,54].

Here we revert to the question what physical implications the extension to magnetic space groups (MSG) symmetries can bring within the above context. To this end, we start by a case study in space group family (SG) 75 and find that within a magnetic background some Wyckhoff positions necessarily imply nontriviality. Turning to antiferromagnetic case we, for the first time, find a model exhibiting fragile and Euler class topology in a MSG and identify the protecting symmetries as well as defining quantities. The magnetic symmetry defining antiferromagnetic (AFM) order is however broken upon adding a generic Zeeman term, giving rise to a ferro/ferrimagnetic-compatible (FM) phase within the same

*adrien.bouhon@gmail.com

†rjs269@cam.ac.uk

 ©2021 American Physical Society

family. The correspondence subsequently manifests itself by conveying that the fragile topological nature has to translate into bands of finite Chern number in the FM counterpart. Going beyond fragile topology, we find that the other remaining possibility of this configuration entails a symmetry protected Weyl semimetallic phase phase, characterized by a quantized π-Berry phase. The stable nodal phase corresponds to finite $\mathbf{Z}_2$ symmetry indicator [35] that is protected by the combination of the C_4 and C_2T symmetries. We moreover show that this phase possesses a systematic correspondence to a nontrivial Chern insulating FM counterpart at half-filling, characterized by an even Chern number $\mathcal{C} = 2 \bmod 4$. We then generalize our findings by formulating an exhaustive list of tetragonal MSGs featuring this necessarily present topological configurations and their systematic correspondences relating AFM and FM counterparts. We moreover address the effect of adding and removing unitary symmetries leading to the identification of magnetic Dirac points [55], and the generalization of the C_2T protected Weyl semi-metallic phases to numerous MSGs. Most importantly, we find that this mechanism can occur on planes in 3D systems that were previously diagnosed as trivial. At the crux of the argument lies that the in-plane topology must coexist with symmetry indicated nodes away from the subdimensional regions, such that the 3D conditions appear trivial. Nonetheless, these *subdimensionally enriched topological nodal topologies* exhibit robust topological features, such as corner modes plus Fermi arcs in the subdimensional gapped fragile AFM case [56], or Fermi arcs plus Fermi arcs in the subdimensional Weyl nodal AFM case, and thus pinpoint to a new class of gapped-nodal topological materials to explore.

II. MAGNETIC SPACE GROUP AND MAGNETIC STRUCTURE: A FIRST CASE STUDY IN SG P4 (NO. 75)

To concretize matters we depart from a simple model for the tetragonal magnetic space group P_C4 (MSG No. 75.5 using the BNS convention) [57,58]. The MSG can be decomposed into left cosets as $\mathcal{G}_{75.5}/\mathcal{G}_{75.1} = (E|0)\mathcal{G}_{75.1} + (E|\tau)'\mathcal{G}_{75.1}$, where the space group $\mathcal{G}_{75.1} = C_4 \times \mathbf{T}$ ($P4$, No. 75.1 in the BNS convention) has no antiunitary symmetry [57] (E is the identity, the prime $(\cdot)'$ stands for time reversal, and $\tau = \boldsymbol{a}_1/2 + \boldsymbol{a}_2/2$). MSG75.1 (P4) has point group C_4 with the normal subgroup of translations $\mathbf{T}$ corresponding to the primitive tetragonal Bravais lattice $\{n_1\boldsymbol{a}_1 + n_2\boldsymbol{a}_2 + n_3\boldsymbol{a}_3\}_{n_1,n_2,n_3\in\mathbb{Z}}$ where the primitive vectors are $\boldsymbol{a}_1 = a(1,0,0)$, $\boldsymbol{a}_2 = a(0,1,0)$, and $\boldsymbol{a}_3 = c(0,0,1)$. In the following, we first focus on the two-dimensional projection $z = 0$, namely we study the corresponding magnetic layer group p_c4 (denoted MLG49.4.357 in [58]). In addition, we use the fact that MSG75.5 (P_C4) is generated by $(C_{4z}|0)\mathbf{T}$ (C_{4z} is the rotation by $\pi/2$ around the z-axis in the positive trigonometric orientation) and $(E|\tau)'\mathbf{T}$ (we will call $(E|\tau)'$ a *nonsymmorphic* time reversal symmetry (TRS) as it contains a fractional translation).

Generally, magnetic space groups with *nonsymmorphic TRS*, called Shubnikov space groups of type IV [57], correspond to AFM structure. Writing $(\boldsymbol{r}, \boldsymbol{m})$ for a magnetic moment $\boldsymbol{m}$ located at $\boldsymbol{r}$, the action of $(E|\tau)'$ gives ${}^{(E|\tau)'}(\boldsymbol{r}, \boldsymbol{m}) = (\boldsymbol{r} + \tau, -\boldsymbol{m})$, and the square ${}^{[(E|\tau)']^2}(\boldsymbol{r}, \boldsymbol{m}) = (\boldsymbol{r} + \boldsymbol{a}_1 + \boldsymbol{a}_2, \boldsymbol{m})$, i.e., the moment is conserved under translation by a Bravais lattice vector while it is flipped under a fractional translation. Hence MSG75.5 (P_C4) is compatible with the AFM structure drawn over one unit cell in Fig. 1(a), where all the moments of equal sign (pointing in the direction of the vertical $\hat{z}$ axis) are obtained under the action of elements generated by $(C_{4z}|0)\mathbf{T}$. In the following, we assume the existence of a magnetic background and describe its effect on the band structure's topology of itinerant electrons. We note that such magnetism can be obtained directly as localized atomic magnetism within density functional theory frameworks [59], or as the solution of an effective spin Hamiltonian mapped from the Green's functions of interacting electrons [60,61]. Alternatively, effective electronic tight-binding Hamiltonians were derived from the double exchange model, i.e., non-self-interacting electrons coupled through Hund's coupling to local classical magnetic moments that interact via super-exchange coupling [62], where the electron spins antialign with the local moments, and for which line-nodal semimetallic phases were recently discussed [63].

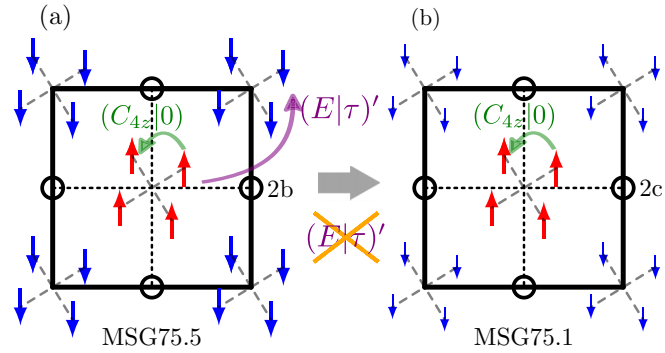

FIG. 1. Background magnetic structures for MSG75.5 and 75.1 with Wyckoff positions of interest indicated in standard notation. The latter MSG is effectively realized by making the oppositely-oriented moments (red/blue spins aligned with the $\hat{z}$ axis perpendicular to the plane) in the former of unequal magnitude. This thus relates an antiferromagnetic-compatible configuration of the SG75-family with a ferro/ferrimagnetic one.

A. Necessary crystalline fragile antiferromagnetic topology

Adopting maximal Wyckoff position $2b$ [58], spanned by the sublattice sites $\boldsymbol{r}_A = \boldsymbol{a}_1/2$ and $\boldsymbol{r}_B = \tau - \boldsymbol{r}_A = \boldsymbol{a}_2/2$, and setting one s-electronic orbital and both spin-z-1/2 components per site, we define the corresponding Bloch orbital basis functions

$$|\varphi_{\alpha,\sigma}, \boldsymbol{k}\rangle = \sum_{\boldsymbol{R}\in\mathbf{T}} e^{i\boldsymbol{k}\cdot(\boldsymbol{R}+\boldsymbol{r}_\alpha)}|w_{\alpha,\sigma}, \boldsymbol{R} + \boldsymbol{r}_\alpha\rangle, \tag{1}$$

with $\alpha = A, B$ and $\sigma = \uparrow, \downarrow$ (taking $\hat{z}$ as the quantization axis of the spins). Ordering the degrees of freedom as $\boldsymbol{\varphi} = (\varphi_{A,\uparrow}, \varphi_{A,\downarrow}, \varphi_{B,\uparrow}, \varphi_{B,\downarrow})$, the generators of MSG75.5 (P_C4), i.e., C_{4z} rotation and nonsymmorphic time reversal, are then represented through

$$\begin{aligned}\langle\boldsymbol{\varphi}, D_{\pi/2}\boldsymbol{k}|^{(C_{4z}|0)}|\boldsymbol{\varphi}, \boldsymbol{k}\rangle &= (\sigma_x \otimes M_4),\\ \langle\boldsymbol{\varphi}, -\boldsymbol{k}|^{(E|\tau)'}|\boldsymbol{\varphi}, \boldsymbol{k}\rangle &= e^{i\boldsymbol{k}\cdot\tau}(\sigma_x \otimes -i\sigma_y)\mathcal{K},\end{aligned} \tag{2}$$

where $M_4 = \mathrm{diag}[e^{-i\pi/4}, e^{i\pi/4}]$, and $D_{\pi/2}$ is the 3D rotation matrix by an angle $\pi/2$ around the k_z axis, $\{\sigma_i\}_{i=x,y,z}$ are the Pauli matrices, and $\mathcal{K}$ is complex conjugation. Combining the two generators, we also obtain

$$\langle \boldsymbol{\varphi}, -D_{\pi/2}\boldsymbol{k}|^{(C_{4z}|\tau)'}|\boldsymbol{\varphi}, \boldsymbol{k}\rangle = e^{iD_{\pi/2}\boldsymbol{k}\cdot\boldsymbol{\tau}}(\mathbb{1}\otimes -i\sigma_y M_4^*)\mathcal{K}. \quad (3)$$

It follows that the orbit of the action of the symmetries $\{(E|0), (C_{4z}|0), (E|\tau)', (C_{4z}|\tau)'\}$ on $\varphi_{A,\uparrow}$ is $\{\varphi_{A,\uparrow}, \varphi_{A,\downarrow}, \varphi_{B,\uparrow}, \varphi_{B,\downarrow}\}$, i.e., all four degrees of the freedom are intertwined by the symmetries of MSG75.5 (P_C4). It can be easily checked that this remains true for any change of basis (i.e., under any general rotation among the sublattice and spinor components). Furthermore, it can be verified that the atomic orbitals cannot be moved to any other Wyckoff position without breaking the symmetries. We therefore conclude that $\{|\boldsymbol{\varphi}, \boldsymbol{k}\rangle\}_{\boldsymbol{k}\in \mathrm{BZ}}$ defines a four dimensional *elementary band representation* (EBR) [25,64–66] as it is formed by the *minimal* set of localized (atomic like) orbitals at the sites $2b$ that is compatible with the magnetic space group symmetries, and we denote it $\mathrm{EBR}^{2b}_{75.5}$. This agrees with Ref. [36] which lists $2b$ as a maximal Wyckoff position and excludes this EBR from the exceptional composite EBRs.

A minimal tight-binding model for $\mathrm{EBR}^{2b}_{75.5}$ is given by

$$\begin{aligned} H(\boldsymbol{k}) = {} & t_1 f_1(\boldsymbol{k})\sigma_z \otimes \sigma_z \\ & + t_2 f_2(\boldsymbol{k})\sigma_y \otimes \mathbb{1} + t_3 f_3(\boldsymbol{k})\sigma_x \otimes \mathbb{1} \\ & + \lambda_1 g_1(\boldsymbol{k})\mathbb{1}\otimes\sigma_+ + \lambda_1^* g_1^*(\boldsymbol{k})\mathbb{1}\otimes\sigma_- \\ & + \lambda_2 g_2(\boldsymbol{k})\sigma_x\otimes\sigma_+ + \lambda_2^* g_2^*(\boldsymbol{k})\sigma_x\otimes\sigma_-, \end{aligned} \quad (4)$$

with $\sigma_\pm = (\sigma_x \pm i\sigma_y)/2$ and the lattice form factors

$$\begin{aligned} f_1 &= \cos \boldsymbol{a}_1\boldsymbol{k} - \cos \boldsymbol{a}_2\boldsymbol{k}, \quad g_1 = \sin \boldsymbol{a}_1\boldsymbol{k} - i\sin \boldsymbol{a}_2\boldsymbol{k}, \\ f_2 &= \cos \boldsymbol{\delta}_1\boldsymbol{k} - \cos \boldsymbol{\delta}_2\boldsymbol{k}, \quad g_2 = \sin \boldsymbol{\delta}_1\boldsymbol{k} - i\sin \boldsymbol{\delta}_2\boldsymbol{k}, \\ f_3 &= \cos \boldsymbol{\delta}_1\boldsymbol{k} + \cos \boldsymbol{\delta}_2\boldsymbol{k}, \end{aligned} \quad (5)$$

defined in terms of the bond vectors $\boldsymbol{\delta}_{\binom{1}{2}} = (\boldsymbol{a}_1 \binom{-}{+} \boldsymbol{a}_2)/2$. It is assumed that $\{t_1, t_2, t_3\}$ are real, while $\{\lambda_1, \lambda_2\}$ can be complex. In the following, we first set $t_1, t_2, t_3 = 1$, and $\lambda_1, \lambda_2 = (1/2)e^{i\pi/5}$.

Of importance for the analysis of the band structure and its topology are the squares of the twofold antiunitary symmetries [67,68]. The nonsymmorphic time reversal squares as

$$\langle \boldsymbol{\varphi}, \boldsymbol{k}|^{[(E|\tau)']^2}|\boldsymbol{\varphi}, \boldsymbol{k}\rangle = -e^{-i\boldsymbol{k}\cdot 2\tau}\mathbb{1}_{4\times 4}, \quad (6)$$

from which we get

$$\langle \boldsymbol{\varphi}, \Gamma|^{[(E|\tau)']^2}|\boldsymbol{\varphi}, \Gamma\rangle = \langle \boldsymbol{\varphi}, M|^{[(E|\tau)']^2}|\boldsymbol{\varphi}, M\rangle = -\mathbb{1}_{4\times 4}. \quad (7)$$

We thus conclude that there must be a twofold Kramers degeneracy at Γ and M, and we call them TRIM (time reversal invariant momentum) in the following. Combining the nonsymmorphic time reversal with C_{2z}, we get $(C_{2z}|\tau)'$ that is represented through

$$\langle \boldsymbol{\varphi}, -C_{2z}\boldsymbol{k}|^{(C_{2z}|\tau)'}|\boldsymbol{\varphi}, \boldsymbol{k}\rangle = e^{iD_\pi \boldsymbol{k}\cdot\boldsymbol{\tau}}(\sigma_x \otimes i\sigma_x)\mathcal{K} \quad (8)$$

TABLE I. Character table for the magnetic space group IRREPs of MSG75.1 ($P4$), and coIRREPs of the unitary symmetries of MSG75.5 (P_C4), at Γ, M, and X, with $\omega = e^{i\pi/4}$. The coIRREPs of MSG75.5 (P_C4) are given by the pairing of the two IRREPs of MSG75.1 ($P4$) within the same column (e.g., $\overline{\Gamma}_5\overline{\Gamma}_7 = \overline{\Gamma}_5 \oplus \overline{\Gamma}_7$). Retrieved from the Bilbao Crystallographic Server [69]. The second column gives the spin components located at the Wyckoff position $2c$ of MSG75.1 ($P4$) from which the IRREPs are induced.[a]

	WP $2c$	$\overline{\Gamma}_5$ $\overline{\Gamma}_7$	$\overline{\Gamma}_6$ $\overline{\Gamma}_8$	$\overline{M}_8$ $\overline{M}_5$	$\overline{M}_7$ $\overline{M}_6$	$\overline{X}_3$	$\overline{X}_4$
C_{4z}	$\uparrow_z$	$-\omega^*$	ω^*	ω	$-\omega$		
	$\downarrow_z$	$-\omega$	ω	$-\omega^*$	ω^*		
C_{2z}	$\uparrow_z$	$-i$	$-i$	i	i	-i	i
	$\downarrow_z$	i	i	$-i$	$-i$		

[a]We note that for any maximal Wyckoff position (WP) of MSG75.1 ($P4$) $\{1a, 1b, 2c\}$ [36,69] the spin-z components are good quantum numbers at Γ and M, which originates from the fact that the vertical C_{4z}-axes (for WPs $1a$ and $1b$) and C_{2z} axes (for WPs $2c$) give natural quantization axes for the spins. At the Wyckoff position $2c$ (compatible with the Wyckoff position $2b$ of MSG75.5), the spin-z $+1/2$ $(+3/2)$ induces $\{\overline{\Gamma}_5, \overline{\Gamma}_6, \overline{M}_7, \overline{M}_8\}$, and the spin-$z$ $-1/2$ $(-3/2)$ induces $\{\overline{\Gamma}_7, \overline{\Gamma}_8, \overline{M}_5, \overline{M}_6\}$.

and squares as

$$\langle \boldsymbol{\varphi}, \boldsymbol{k}|^{[(C_{2z}|\tau)']^2}|\boldsymbol{\varphi}, \boldsymbol{k}\rangle = \mathbb{1}_{4\times 4}. \quad (9)$$

The existence of such an antiunatry symmetry that leaves the momentum invariant and squares to $+1$ implies that there exists a change of orbital basis in which the Hamiltonian is real symmetric [52]. This is here achieved through $\widetilde{H}(\boldsymbol{k}) = V \cdot H(\boldsymbol{k}) \cdot V^\dagger$ where $V = \sqrt{\sigma_x \otimes i\sigma_x}$. We symbolically refer to this symmetry as the "C_2T" symmetry.

The bands are then effectively analyzed using the (co-)irreducible representations at the Γ, M, and X points. These are summarized in Table I (and discussed further in Appendix D 1).

Whenever a band structure of an EBR may be split by an energy gap, at least one band subspace must be topological, namely, either both band subspaces are stable or fragile topological, or one is trivial and the other must be fragile topological [25,37,38]. Heuristically this is the case because there must be an obstruction forbidding the mapping of Bloch eigenstates of EBR subspaces to localized Wannier functions (i.e., atomic limits) as a result of the space group symmetries, since the dimensionality of any band subspace's Wannier basis (here two) is necessarily smaller than the dimensionality of the by definition minimal EBR (here four). As a consequence, the Wannier functions representing an EBR's subspace are either delocalized if we impose all symmetry constraints, or are incompatible with the space group symmetries. From the induced irreducible co-representations (coIRREPs) and the compatibility relations among these [23,69,70], we conclude that $\mathrm{EBR}^{2b}_{75.5}$ can be split over all high-symmetry regions of the Brillouin zone. We actually obtain a gapped band structure over the whole Brillouin zone in our minimal model, see Figs. 2(a) and 2(b) that gives the ordering in energy of the

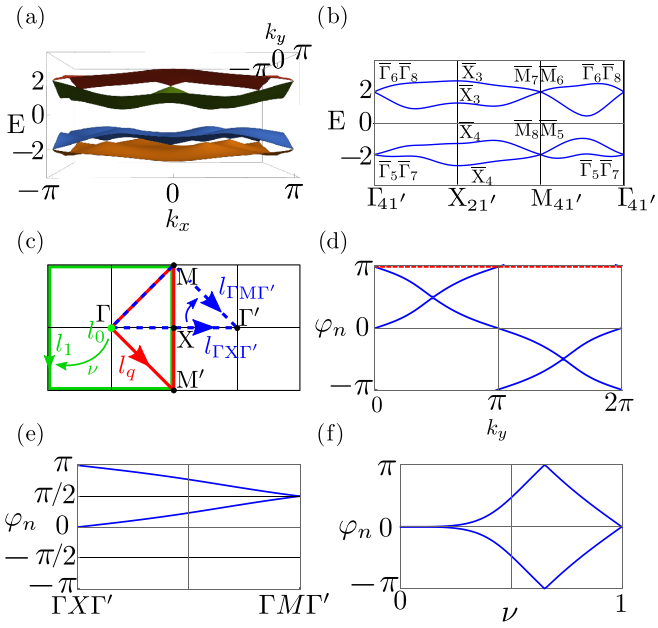

FIG. 2. Nontriviality in MSG75.5. (a) Full band structure of model defined in Eq. (4) and (b) along the high-symmetry directions with coIRREPs indicated. (c) Symmetry-based paths within the Brillouin zone used as base loops for the patch Wilson loop (dashed blue), the C_4-symmetric Wilson loop (green), and the symmetry indicated Berry phase (red). The small arrows show the direction of flow (deformation of base loops). (d) Two-band Wilson loop (blue lines), integrated along $k_x \in [0, 2\pi]$, and total Berry phase (red dashed line) for the valence (equivalently, conduction) bands of $\mathrm{EBR}^{2b}_{75.5}$. Integrating along $k_y \in [0, 2\pi]$ gives equivalent results. (e) Wilson loop flow over a patch from the base loop $\Gamma X \Gamma'$ to $\Gamma M \Gamma'$. (f) C_4-symmetric Wilson loop flow from the point $l_0 = \Gamma$ to the boundary of the Brillouin zone, $l_1 = \partial\mathrm{BZ}$. Notation follows conventions of the main text.

induced coIRREPs[1] (defined in Table I). The rational behind the splitting of the EBR will be explained when we address the symmetry indicator, which turns out to be trivial for the IRREPs ordering of Fig. 2(b). In the following we refer to the lower (higher) two-band subspace as the *valence* (*conduction*) subspace at half-filling. The question is then to determine the topology of each gapped subspace as in that case there is no stable symmetry indicated topology.

As pointed out above, the C_2T symmetry implies that the Bloch eigenvectors can be made real through the appropriate change of basis. It follows that (oriented) two-band subspaces of such Hamiltonians are topologically classified by Euler class $\chi \in \mathbb{Z}$ that can be computed as a winding of Wilson loop [38,47–49,52]. We find that the Wilson loop ($\mathcal{W}[l]$, see Appendix A) of each two-band subspace winds along both directions (i.e., integrating along the base path $l_{k_y} = \{(k_x, k_y)|k_x \in [0, 2\pi]\}$ and scanning through $k_y \in [0, 2\pi]$, and similarly if we exchange $k_x \leftrightarrow k_y$), see Fig. 2(d). We moreover find that the Berry phase ($e^{i\gamma_B[l]} = \mathrm{Det}\mathcal{W}[l]$) of both two-band

TABLE II. Character table for the magnetic space group IRREPs of MSG77.13 ($P4_2$), and coIRREPs of the unitary symmetries of MSG77.18 (P_I4_2), at Z, A, and R, with $\omega = e^{i\pi/4}$. The (co-)IRREPs at Γ, M, and X are the same as in Table I. The coIRREPs of MSG77.18 are given by the pairing of the two IRREPs of MSG77.13 within the same column. Retrieved from the Bilbao Crystallographic Server [69].

	WP	$\overline{Z}_5$	$\overline{Z}_6$	$\overline{A}_8$	$\overline{A}_7$		
	$2c$	$\overline{Z}_8$	$\overline{Z}_7$	$\overline{A}_5$	$\overline{A}_6$	$\overline{R}_3$	$\overline{R}_4$
$(C_{4z}\|\tau_3)$	$\uparrow_z$	$-\omega$	ω	ω^*	$-\omega^*$		
	$\downarrow_z$	$-\omega^*$	ω^*	$-\omega$	ω		
$(C_{2z}\|0)$	$\uparrow_z$	$-i$	$-i$	i	i	-i	i
	$\downarrow_z$	i	i	$-i$	$-i$		

subspaces is π along both directions, see Fig. 2(d) (red dashed line), pointing to the nonorientability of the subspaces' frames of Bloch eigenvectors [49]. While the Euler class is not defined strictly speaking for an *un*orientable band subspace [71], we still obtain the winding of Wilson loop as an element of $\pi_1(\mathrm{O}(2)) = \mathbb{Z}$ since $\mathcal{W}[l] \in \mathrm{O}(2)$ when computed in the real gauge (i.e., using the Bloch eigenvectors of the real symmetric form).[2] We thus conclude that each two-band subspace has a nonorientable nontrivial fragile topology [49]. Moreover, we also point out that the nontrivial π Berry-phases are actually appealing from a bulk-boundary perspective [72]. Indeed, they culminate in-gap edge states, reflecting a physical signature, see Ref. [56] for a detailed analysis.

We further derive in Appendix A the necessary nontriviality of the split $\mathrm{EBR}^{2b}_{75.5}$. Following Ref. [38], we show that the crystal symmetries impose a finite fractional winding of Wilson loop over one quarter of the Brillouin zone, i.e., the patch bounded by the paths $\Gamma X \Gamma'$ and $\Gamma M \Gamma'$ (blue dashed lines) in Fig. 2(c). This results from the difference in the symmetry protected quantizations of the Wilson loops over the two base paths, i.e., $\mathrm{Arg}[\mathrm{eig}\{\mathcal{W}[l_{\Gamma X \Gamma'}]\}] = [0, \pi]$ and $\mathrm{Arg}[\mathrm{eig}\{\mathcal{W}[l_{\Gamma M \Gamma'}]\}] = [\pi/2, \pi/2]$, which depends on both the IRREPs and the spinor structure of the bands (i.e., spin-parallel versus spin-flip parallel transports, see Appendix A), as is also verified through direct numerical evaluation of the Wilson loop over the patch in Fig. 2(e). Then, by C_4 symmetry, the Wilson loop must have a finite integer winding over the whole Brillouin zone, as confirmed by Fig. 2(d). We later refer to it as the *crystalline Euler fragile topology* (written CEF in Table III) when we address the generalization to other MSGs.

We furthermore compute the C_4-symmetric Wilson loop flow [38,73,74] from the point $l_0 = \Gamma$ to the contour of the Brillouin zone $l_1 = \partial\mathrm{BS}$, shown in green in Fig. 2(c), and between which we extrapolate by taking the scaled contour $\nu\partial\mathrm{BZ}$ for $\nu \in [0, 1]$. This also exhibits a full winding shown in Fig. 2(f). The C_4-symmetric Wilson loop winding alludes to the persistence of nontrivial fragile topology after breaking

[1]The coIRREPs of MSG75.5 are obtained from the IRREPs of MSG75.1 with the degeneracies imposed by the extra antiunitary symmetries (this is practically determined by the Herring rule [57]).

[2]Strictly speaking there is reduction $\mathbb{Z} \to \mathbb{N}$ of the classification as a consequence of the facts that band subspaces are *orientable* and not *oriented*, and that the homotopy classes of gapped Hamiltonians have no fixed base points [49].

TABLE III. Candidate MSGs for the (Euler) fragile/stable-nodal AFM to Chern FM mechanism, including those profiting from the subdimensional topological analysis. The table lists the AFM and corresponding FM counterparts as well as their time reversal invariant momenta (TRIM) which host Kramers doublets (i.e., Weyl nodes). Moreover, it details the topology by enumerating the value of $C_2T = \pm 1$ and the two-band subspace (2-BS) characterization on the $k_z = 0, \pi$ momentum planes. $[C_2T]^2 = +1$ indicates Euler class (real) topology, while $[C_2T]^2 = -1$ implies the twofold Kramers degeneracy of the bands. The labels CEF, CF, CW, and CC indicate crystalline Euler fragile (with symmetry-indicated Wilson loop quantization), crystalline fragile (with the winding of C_4-symmetric Wilson loop), and crystalline Weyl semimetallic (with a symmetry-indicated π-Berry phase), respectively. When the 2-BS Topology is CW, we mean that there must be Weyl nodes connecting adjacent two-band subspaces. When we write CEF/CW, we mean that either of the topologies is realized depending on the ordering of IRREPs. Finally, the EBR column specifies the elementary band representations[a] hosting the topology[b]. All FM candidates acquire crystalline Chern (CC) topology when obtained from their AFM parents through Zeeman splitting. The EBR data were retrieved from the Bilbao Crystallographic Server [69].

AFMSG	TRIM	k_z	$[C_2T]^2$	2-BS Topology	EBRs	FMSG
75.4 (P_c4)	Γ, M, X, X'	0	+1	*CEF*	$(2a, \uparrow_z) \oplus (2a, \downarrow_z)$, $(2b, \uparrow_z) \oplus (2b, \downarrow_z)$,	75.1 ($P4$)
		π	−1	*CF*	$(4c, \uparrow_z)$, $(4c, \downarrow_z)$	
75.5 (P_C4)	Γ, M, Z, A	0	+1	*CEF/CW*	$(2a, \uparrow_z) \oplus (2a, \downarrow_z)$, $(2b, \uparrow_z \oplus \downarrow_z)$,	75.1 ($P4$)
		π	+1	*CEF/CW*	$(4c, \rightarrow_y)$	
75.6 (P_I4)	Γ, M, R, R'	0	+1	*CEF/CW*	$(2a, \uparrow_z^{1/2}) \oplus (2a, \downarrow_z^{1/2}) \oplus (2a, \uparrow_z^{3/2}) \oplus (2a, \uparrow_z^{3/2})$,	75.1 ($P4$)
		π	−1	*CF*	$(4b, \uparrow_z)$, $(4b, \downarrow_z)$	
76.10 (P_c4_1)	Γ, M, X, X'	0	+1	*CEF*	$(4a, \rightarrow_y)$, $(4b, \rightarrow_y)$, $(4c, \rightarrow_y)$	76.7 ($P4_1$)
		π	+1	*CEF/CW*		
76.11 (P_C4_1)	Γ, M, Z, A	0	+1	*CEF/CW*	$(8a, \rightarrow_y)$	76.7 ($P4_1$)
		π	−1	*CF*		
76.12 (P_I4_1)	Γ, M, R, R'	0	+1	*CEF/CW*	$(4a, \rightarrow_y)$	76.7 ($P4_1$)
		π	+1	*CEF/CW*		
77.16 (P_c4_2)	Γ, M, X, X'	0	+1	*CEF*	$(2a, \uparrow_z \oplus \downarrow_z)$, $(2b, \uparrow_z \oplus \downarrow_z)$,	77.13 ($P4_2$)
		π	−1	*CF*	$(4c, \uparrow_z)$, $(4c, \downarrow_z)$	
77.17 (P_C4_2)	Γ, M, Z, A	0	+1	*CEF/CW*	$(4a, \uparrow_z) \oplus (4a, \downarrow_z)$, $(4b, \uparrow_z) \oplus (4b, \downarrow_z)$,	77.13 ($P4_2$)
		π	+1	*CEF/CW*	$(4c, \rightarrow_y)$	
77.18 (P_I4_2)	Γ, M, R, R'	0	+1	*CEF/CW*	$(2a, \uparrow_z \oplus \downarrow_z)$, $(4b, \uparrow_z) \oplus (4b, \downarrow_z)$	77.13 ($P4_2$)
		π	−1	*CF*		
78.22 (P_c4_3)	Γ, M, X, X'	0	+1	*CEF*	$(4a, \rightarrow_y)$, $(4b, \rightarrow_y)$, $(4c, \rightarrow_y)$	78.19 ($P4_3$)
		π	+1	*CEF/CW*		
78.23 (P_C4_3)	Γ, M, Z, A	0	+1	*CEF/CW*	$(8a, \rightarrow_y)$	78.19 ($P4_3$)
		π	−1	*CF*		
78.24 (P_I4_3)	Γ, M, R, R'	0	+1	*CEF/CW*	$(4a, \rightarrow_y)$	78.19 ($P4_3$)
		π	+1	*CEF/CW*		
79.28 (I_c4)	Γ, M, X, X'	0	+1	CEF	$(4a, \uparrow_z) \oplus (4a, \downarrow_z)$, $(4b, \uparrow_z \oplus \downarrow_z)$, $(8c, \rightarrow_y)$	79.25 ($I4$)
80.32 (I_c4_1)	Γ, M, X, X'	0	+1	CEF	$(8a, \rightarrow_y)$, $(8b, \rightarrow_y)$, $(8c, \uparrow_z)$, $(8c, \downarrow_z)$	80.29 ($I4_1$)
81.36 ($P_c\bar{4}$)	Γ, M, X, X'	0	+1	*CEF*	$(2a, \uparrow_z) \oplus (2a, \downarrow_z)$, $(2c, \uparrow_z) \oplus (2c, \downarrow_z)$,	81.33 ($P\bar{4}$)
		π	−1	*CF*	$(4g, \uparrow_z)$, $(4g, \downarrow_z)$	
81.37 ($P_C\bar{4}$)	Γ, M, Z, A	0	+1	*CEF/CW*	$(2a, \uparrow_z^{1/2}) \oplus (2a, \downarrow_z^{1/2}) \oplus (2a, \uparrow_z^{3/2}) \oplus (2a, \uparrow_z^{3/2})$, $(2b, \uparrow_z^{1/2}) \oplus (2b, \downarrow_z^{1/2}) \oplus (2b, \uparrow_z^{3/2}) \oplus (2b, \uparrow_z^{3/2})$,	81.33 ($P\bar{4}$)
		π	+1	*CEF/CW*	$(2c, \uparrow_z \oplus \downarrow_z)$, $(2d, \uparrow_z \oplus \downarrow_z)$, $(4g, \rightarrow_y)$	
81.38 ($P_I\bar{4}$)	Γ, M, R, R'	0	+1	*CEF/CW*	$(2a, \uparrow_z^{1/2}) \oplus (2a, \downarrow_z^{1/2}) \oplus (2a, \uparrow_z^{3/2}) \oplus (2a, \downarrow_z^{3/2})$, $(2b, \uparrow_z^{1/2}) \oplus (2b, \downarrow_z^{1/2}) \oplus (2b, \uparrow_z^{3/2}) \oplus (2b, \downarrow_z^{3/2})$,	81.33 ($P\bar{4}$)
		π	−1	*CF*	$(2c, \uparrow_z \oplus \downarrow_z)$, $(2d, \uparrow_z \oplus \downarrow_z)$	
82.42 ($I_c\bar{4}$)	Γ, M, X, X'	0	+1	CEF	$(4a, \uparrow_z) \oplus (4a, \downarrow_z)$, $(4d, \uparrow_z) \oplus (4d, \downarrow_z)$, $(8g, \rightarrow_y)$	82.39 ($I\bar{4}$)

[a]The EBRs are defined for a given Wyckoff position and a fixed spin basis. We either take the vertical $\hat{z}$-axis (C_4-axis) as the quantization axis for the spin-1/2 (3/2) with the spin basis $(\uparrow_z, \downarrow_z)$, or we take a quantization axis that is perpendicular to $\hat{z}$, e.g., $\hat{y}$ for which the spin basis is $(\rightarrow_y, \leftarrow_y) = (\uparrow_z + \mathrm{i} \downarrow_z, \mathrm{i} \uparrow_z + \downarrow_z)/\sqrt{2}$.

[b]In the case of a single EBR, splitable at $k_z = 0$ and $k_z = \pi$, we mean that it *must* host one of the listed nontrivial topologies. In the case of a (direct) sum of EBRs, we mean that the topology *can* be achieved through the permutation of IRREPs between the EBRs.

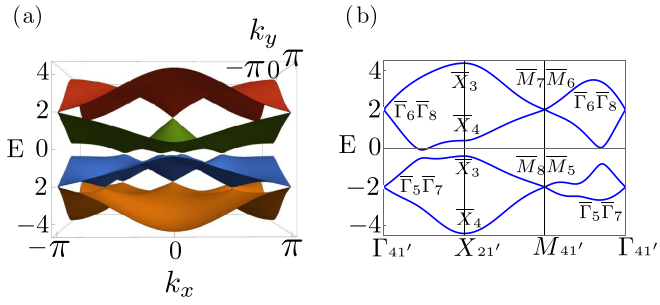

FIG. 3. Stable topological semimetallic phase of MSG75.5 (P_C4) indicated by $z_2 = 1 \bmod 2$, here represented by $\mathrm{EBR}^{2b}_{75.5}$ at half-filling. Full band structure over (a) BZ and (b) along high-symmetry lines where two coIRREPs at X have been inverted when compared to Fig. 2(b).

$(C_{2z}|0)'$ symmetry, i.e., without Euler class. We refer to it as the *crystalline fragile topology* (written CF in Table III).

These results thus constitute three complementary ways to reveal the *necessary nontriviality* of the crystalline fragile topology of the split $\mathrm{EBR}^{2b}_{75.5}$.

B. Stable nodal topological phases

We can characterize the symmetry indicators of a given band structure by using the matrix containing all allowed magnetic EBRs. This results in a $\mathbb{Z}_2$ indicator for MSG75.5 (P_C4). As detailed in Appendix D, the explicit expression for this indicator is

$$z_2 = n_{\overline{X}_3} \bmod 2, \tag{10}$$

where $n_{\overline{X}_3}$ is the number of occupied bands at the X point with the IRREP $\overline{X}_3$. In agreement with the discussion in the previous section, the indicator is trivial for the fragile phase of $\mathrm{EBR}^{2b}_{75.5}$ at half-filling, as can be verified from the coIREPs of Fig. 2(b). We emphasize that this symmetry indicator readily generalizes for an arbitrary even number of occupied bands, i.e., at a filling $\nu \in 2\mathbb{Z} + 2$.

We thus conclude that a stable topological phase can be reached through a band inversion at X. This is achieved for the model Eq. (4) by taking $|\lambda_2| > \sqrt{2}|t_1|$. Setting $\lambda_2 = (6/5)\sqrt{2}$, we obtain the band structure of Fig. 3 that exhibits a semimetallic phase with four nodal points around Γ at half-filling. We find that the stable symmetry indicator z_2 corresponds to a π Berry phase for the valence (conduction) bands along the path l_q [see Fig. 2(c)], i.e., (see derivation in Appendix B)

$$\begin{aligned}
\gamma_B^{(1::2)}[l_q] &= -\mathrm{i}\ln[\mathrm{Det}(\mathcal{W}^{(1::2)}[l_q])] \\
&= -\mathrm{i}\ln\left[\frac{\xi_4^{\Gamma}(1)\xi_4^{\Gamma}(2)\xi_2^{\mathrm{M}}(1)\xi_2^{\mathrm{M}}(2)}{\xi_4^{\mathrm{M}}(1)\xi_4^{\mathrm{M}}(2)\xi_2^{\mathrm{X}}(1)\xi_2^{\mathrm{X}}(2)}\right] \\
&= -\mathrm{i}\ln\left[\frac{(+1)(+1)}{(-1)\xi_2^{\mathrm{X}}(1)\xi_2^{\mathrm{X}}(2)}\right] \\
&= -\mathrm{i}\ln\left[(-1)\xi_2^{\mathrm{X}}(1)\xi_2^{\mathrm{X}}(2)\right] \\
&= \begin{cases} 0 \bmod 2\pi, & \text{if } z_2 = 0, \\ \pi \bmod 2\pi, & \text{if } z_2 = 1. \end{cases}
\end{aligned} \tag{11}$$

Let us first note that, similarly to Eq. (10), Eq. (11) can also be generalized for an arbitrary even number of occupied bands (i.e., a filling $\nu \in 2\mathbb{Z} + 2$). Importantly, C_2T symmetry (with $[C_2T]^2 = +1$) imposes the vanishing of the $U(1)$ Berry curvature over the two-band occupied eigen-subspaces, since within the real basis we have $\mathcal{F} = \mathrm{Pf}[\mathcal{F}]\mathrm{i}\sigma_y$ [52] and thus $\mathrm{tr}\mathcal{F} \equiv 0$. As a consequence, the Chern number of the gapped AFM phase at half-filling is identically zero. From there results that the nontriviality of the Berry phase indicates a nodal phase (i.e., it indicates the obstruction to define a smooth projector on the occupied bands over the whole Brillouin zone due to the presence of topologically stable band crossings with the unoccupied bands), i.e., the necessary existence of an odd number of nodal points inside the domain bounded by l_q. Upon the breaking of the nonsymmorphic TRS, $C_{2z}T$ is also broken, and the π Berry phase indicates a C_4-symmetry protected Chern number at half-filling, or more generally at a filling $\nu \in 2\mathbb{Z} + 2$,

$$\mathcal{C} = 2z_2 \bmod 4. \tag{12}$$

The nontrivial Chern phases are discussed in detail in the next section.

We emphasize that the nodal points at general momenta are not indicated by the compatibility relations. Indeed, these are stabilized by the $(C_{2z}|\tau)'$ symmetry (C_2T) for which there is not an eigenvalue structure. Instead, the C_2T symmetry quantizes the Berry phase to the values $\{0, \pi\}$, with π indicating an odd number of nodes encircled by l_q. Embedded in 3D the nodal points correspond to single Weyl points that are *pinned* on the C_2T invariant plane (i.e., at $k_z = 0$ where $-C_{2z}\boldsymbol{k} = IC_{2z}\boldsymbol{k} = m_z\boldsymbol{k} = \boldsymbol{k}$) by virtue of the chirality-preserving property of C_2T. Indeed, any Weyl point leaving the $k_z = 0$ plane must have a mirror symmetric image with equal chirality by C_2T symmetry. It is therefore forbidden for a single node to leave the plane by conservation of Chern number. We refer to these phases in the 3D context as the *crystalline Weyl topology* (written CW in Table III).

III. AFM-FM CORRESPONDENCE

We now turn to ferro/ferrimagnetic (FM) phases associated with SG75 obtained from the fragile and stable nodal AFM phases discussed above through the breaking of the antiunitary symmetry $(E|\tau)'$, thereby effectively realizing MSG75.1 (P4, Shubnikov type I). This is done in Eq. (4) by adding a Zeeman coupling term $\epsilon_Z(\mathbb{1} \otimes \sigma_z)$. We find that the topology of the FM-compatible phases are necessarily nontrivial, exhibiting Chern numbers constrained by crystalline symmetries that intricately relate to the topology of the AFM counterparts.

We note that the correspondence discussed here must be contrasted from the Chern phases obtained under an external magnetic field [75] which are in general not symmetry indicated.

A. General mechanism

Let us first generally address the AFM-FM correspondence and its physical mechanisms. For this purpose it is worth starting from MSG83.49 (P_C4/m) which is obtained from

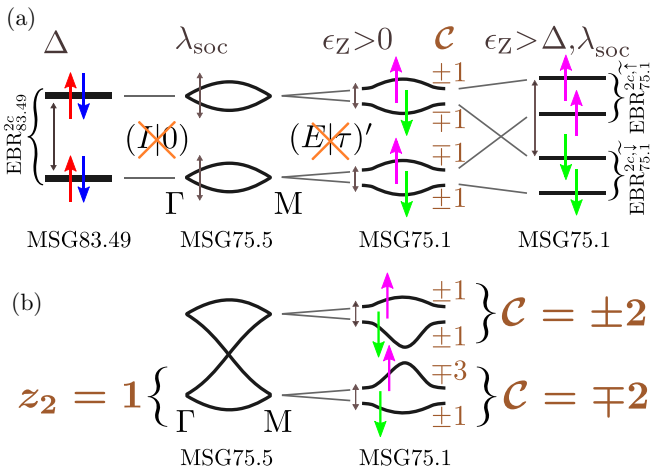

FIG. 4. (a) Splitting and ordering of the EBR's energy levels induced by the successive breaking of inversion $(I|0)$ and nonsymmorphic time reversal $(E|\tau)'$ symmetries. The split $(t_1, t_2, t_3 = \Delta)$ four-dimensional EBR of MSG83.49 (P_C4/m), and MSG75.5 (P_C4) for $z_2 = 0$, separates into *two* split EBRs of MSG75.1 ($P4$) under the combined effect of Dresselhaus-Rashba spin-orbit ($\lambda_1, \lambda_2 = \lambda_{soc}$) and Zeeman ($\epsilon_Z$) couplings, giving rise to energy ordered pseudo-spin-polarized Chern bands ($\mathcal{C} = \text{sign}[t_2]$, brown). Pure spin components are drawn in red and blue (for MSG83.49), pseudo-spin components are drawn in magenta and green for MSG75.1. Under a strong Zeeman splitting, the valence (conduction) subspaces become fully pseudo-spin-polarized (see text) while conserving (at fixed λ_{soc}) the Chern characters of the bands. b) Zeeman splitting when $z_2 = 1$ for the EBR of MSG75.5 (P_C4) leading to a symmetry indicated nontrivial even Chern insulator ($\mathcal{C} = 2 \bmod 4$) at half-filling.

MSG75.5 by simply adding inversion symmetry, i.e., SG83 has point group C_{4h}. The presence of $(I|\tau)'$ symmetry which squares to -1 leads to the twofold Kramers degeneracy of the bands over the whole Brillouin zone. The parent EBR, which we write $\text{EBR}^{2c}_{83.49}$, also splits with a topology characterized by symmetry indicated mirror Chern numbers [36]. We readily obtain the corresponding Hamiltonian by taking $\lambda_1, \lambda_2 = 0$ in Eq. (4). The full splitting of $\text{EBR}^{2c}_{83.49}$ requires $|t_1|, |t_2|, |t_3| > 0$ (which we symbolize by a single variable Δ in Fig. 4), where t_1 is a spin-z-preserving spin-orbit coupling that acts as a delocalized Zeeman coupling on each sublattice orbital but changes sign between sublattice sites, and t_2 and t_3 are spin-preserving inter-sub-lattice site couplings. Due to the basal mirror symmetry $\langle \boldsymbol{\varphi}, m_z \boldsymbol{k}|^{m_z}|\boldsymbol{\varphi}, \boldsymbol{k}\rangle = \mathbb{1} \otimes -i\sigma_z$, each band doublet can be separated into the $-$i and i mirror-eigenvalue sectors, matching with the spin-↑ and spin-↓ components (i.e., the spin z components are good quantum numbers over the whole Brillouin zone).

The terms in $\{\lambda_1, \lambda_2\}$ in Eq. (4) break inversion symmetry and correspond to combined Dresselhaus and Rashba spin-orbit couplings. The effect of the latter (symbolized by λ_{soc}) is to split the Kramers degeneracy away from Γ and M, as represented schematically in Fig. 4(a) for $z_2 = 0$ in Eq. (10). The conservation of Kramers doublets at Γ and M is due to the nonsymmorphic time reversal which still squares to -1 at these points, as derived above. While the bands now have pseudospin components at generic momenta, the pure spin-↑

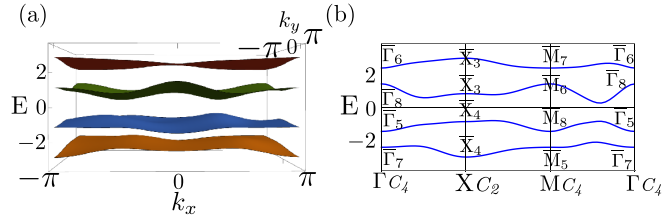

FIG. 5. Nontriviality in MSG75.1. (a) Band structure for MSG75.1 obtained from the model in Eq. (4) together with Zeeman coupling and (b) along high-symmetry lines with the IRREPs indicated. We have taken $\epsilon_Z = 1/2$. Applying Eq. (14) we find that each band hosts a nonzero Chern number.

and spin-↓ components are still good quantum number at Γ and M since the terms in $\lambda_{1,2}$ vanish there.

The AFM-FM transition can then be modeled through a Zeeman term (ϵ_Z) that breaks the nonsymmorphic TRS leading to the splitting of the (Γ and M) Kramers doublets. This leads to the pure spin polarization of the bands at Γ and M since, for any maximal Wyckoff position of MSSG75.1 ($P4$) [36,69], spin-↑ and spin-↓ induce distinct sets of IRREPs at Γ and at M (see the footnote of Table I). In the following we thus refer to the pseudo-spin-polarizations $\widetilde{\uparrow}$ and $\widetilde{\downarrow}$ of the bands in the sense that the band $\widetilde{\uparrow}$ ($\widetilde{\downarrow}$) at $\boldsymbol{k}$ has the pure spin component ↑ (↓) at Γ and M. This does not exclude the case, for dominant spin-flip terms as compared to Zeeman splitting, of a band subspace with an opposite pure spin configuration at Γ (say spin-↑) and M (spin-↓), see the discussion around Eq. (A6) in Appendix A. Such a configuration typically requires long-range spin-flip terms [36]. This results in energy ordered pseudo-spin-polarized Chern bands (column $\epsilon_Z > 0$ in Fig. 4, Fig. 5, and Fig. 12 in Appendix C) with the relative chirality of the minimal model set by sign$[t_2]$. Further increasing Zeeman coupling (while keeping λ_{soc} fixed, see below) leads to fully pseudo-spin-polarized valence and conduction subspaces illustrated in the right column in Fig. 4(a).

As a next step, by switching off the spin-flip $\lambda_{1,2}$ terms, while maintaining a dominant Zeeman splitting, we adiabatically map the fully pseudo-spin-polarized bands into pure spin-polarized split EBRs of MSG75.1 ($P4$). Indeed, the sublattice sites A and B still span a single maximal Wyckoff position, now labeled $2c$ for MSG75.1 ($P4$) [69,76], and from the absence of spin-mixing symmetry we may form spin polarized $\text{EBR}^{2c,\uparrow}_{75.1}$, and $\text{EBR}^{2c,\downarrow}_{75.1}$, from the orbital basis $(\varphi_{A,\uparrow}, \varphi_{B,\uparrow})$, and $(\varphi_{A,\downarrow}, \varphi_{B,\downarrow})$, respectively. We write the adiabatic mapping of the fully pseudo-spin-polarized valence and conduction bands into spin-polarized split EBRs as $\text{EBR}^{2c,\widetilde{\uparrow}}_{75.1} \sim \text{EBR}^{2c,\uparrow}_{75.1}$ and $\text{EBR}^{2c,\widetilde{\downarrow}}_{75.1} \sim \text{EBR}^{2c,\downarrow}_{75.1}$. The symmetry breaking term (Zeeman) thus induces the following phase transition from *one* four-dimensional split EBR (of MSG75.5) to *two* two-dimensional split EBRs (of MSG75.1),

$$\text{EBR}^{2b}_{75.5} \longrightarrow \text{EBR}^{2c,\widetilde{\uparrow}}_{75.1} + \text{EBR}^{2c,\widetilde{\downarrow}}_{75.1} \sim \text{EBR}^{2c,\uparrow}_{75.1} + \text{EBR}^{2c,\downarrow}_{75.1}. \tag{13}$$

We emphasize that this mapping is model independent, in the sense that it continues to exist when we add any extra term in Eq. (4) that satisfies the symmetries of MSG75.5 (P_C4) and MSG75.1 ($P4$). The symmetry broken band structure is

now split into four separated bands and the question is to characterize the topology of each single band.

The symmetry indicated Berry phase for Band n (using the bottom-up labeling of the energy eigenvalues, i.e., $E_n \leqslant E_{n+1}$) along the path $l_q = \Gamma\mathrm{M}'\mathrm{X}\mathrm{M}\Gamma$ (M′=M-$\boldsymbol{b}_2$), see (in red) Fig. 2(a), is [6,13,77] (one-band reduction of Eq. (11), see derivation in Appendix B)

$$\gamma_B^{(n)}[l_q] = -\mathrm{i}\ln\left[\xi_4^{\Gamma}(n)\xi_4^{M}(n)^{-1}\xi_2^{\mathrm{M}}(n)\xi_2^{\mathrm{X}}(n)^{-1}\right], \tag{14}$$

where $\xi_4^{\bar{\boldsymbol{k}}}(n)$ and $\xi_2^{\bar{\boldsymbol{k}}}(n)$ are the C_4- and C_2-eigenvalues, respectively, at the high-symmetry point $\bar{\boldsymbol{k}}$ listed in Table I. The Chern number of Band n, given through $\mathrm{e}^{-\mathrm{i}2\pi\mathcal{C}(n)} = (\mathrm{e}^{\mathrm{i}\gamma_B^{(n)}[l_q]})^4$, is thus

$$\mathcal{C}(n) = -(2/\pi)\gamma_B^{(n)}[l_q] \bmod 4, \tag{15}$$

see also Ref. [36]. We show below that whenever the FM phase is obtained from one of the (necessarily) nontrivial AFM phases of $\mathrm{EBR}_{75.5}^{2b}$, it must be made of nontrivial Chern bands. Remarkably, the Zeeman splitting of the stable nodal phase of MSG75.5 (P_C4), i.e., with $z_2 = 1$ in Eq. (10), necessarily generates a nontrivial Chern FM phases at half-filling, with $\mathcal{C} = 2 \bmod 4$ according to Eq. (12), see Fig. 4(b). This is discussed in detail below where we show that Eq. (12) matches with Eq. (14) and (15) for Band 1 and 2. Below we also use the pseudospin polarization to predict single bands of higher Chern number (i.e., $\mathcal{C} = \pm 3 \bmod 4$) in some regime. In the following we refer to these symmetry indicated Chern phases as the *crystalline Chern topology* (we call it CC topology in the following).

Before we study the AFM to FM phases correspondence for the model Eq. (4) in more detail, we importantly note that the same nontrivial AFM phases, as well as the AFM to FM correspondence, can be obtained from the following EBRs (for MSG75.5 (P_C4) → MSG75.1 ($P4$)):

$$\begin{aligned}\mathrm{EBR}_{2a}^{\uparrow} \oplus \mathrm{EBR}_{2a}^{\downarrow} &\to \mathrm{EBR}_{1a}^{\uparrow} \oplus \mathrm{EBR}_{1b}^{\downarrow} \oplus \mathrm{EBR}_{1a}^{\downarrow} \oplus \mathrm{EBR}_{1b}^{\uparrow},\\ \mathrm{EBR}_{4c}^{\rightarrow} &\to \mathrm{EBR}_{4d}^{\rightarrow},\end{aligned} \tag{16}$$

where $\mathrm{EBR}^{\rightarrow}$ is an EBR formed with noncolinear in-plane spinors $\{(\rightarrow), C_{4z}(\rightarrow), C_{2z}(\rightarrow), C_{4z}^{-1}(\rightarrow)\}$, i.e., with a quantization axis that is perpendicular to the vertical C_4-axis [3] (we chose $\hat{y}$ in Table III with $\rightarrow_y$).

B. Small Zeeman splitting

Here we derive the topology of the FM phases obtained from each of the nontrivial AFM phases of $\mathrm{EBR}_{75.5}^{2b}$ when the Zeeman splitting is small compared to the other energy scales (i.e., $\epsilon_{\mathrm{Z}} < \Delta, \lambda_{\mathrm{SOC}}$ in Fig. 4), underpinning the general mechanism outlined previously.

1. Crystalline Chern ferro/ferrimagnetic topology from fragile AFM phase

Starting from the gapped fragile phase of $\mathrm{EBR}_{75.5}^{2b}$ ($z_2 = 0$) and given the sign of the Zeeman coupling ($\epsilon_{\mathrm{Z}} > 0$, i.e., $E_{\uparrow_z} > E_{\downarrow_z}$) we predict the ordering in energy of the IRREPs of each split Kramers degeneracy to be $E(\overline{\Gamma}_7) < E(\overline{\Gamma}_5) < E(\overline{\Gamma}_8) < E(\overline{\Gamma}_6)$, and $E(\overline{M}_5) < E(\overline{M}_8) < E(\overline{M}_6) < E(\overline{M}_7)$. We show the band structure for MSG75.1 in Figs. 5(a) and 5(b) together with the IRREPs along high-symmetry lines thus confirming the IRREPs ordering.

Substituting the symmetry eigenvalues in Eq. (14), we then readily find $\mathcal{C}(1) = \mathcal{C}(4) = +1 \bmod 4$, and $\mathcal{C}(2) = \mathcal{C}(3) = -1 \bmod 4$. We conclude that each split $\mathrm{EBR}_{75.1}^{2c}$ has a stable Chern class topology. This is confirmed by direct evaluation of the flow of Berry phase for each band, see Fig. 12 in Appendix C.

2. Crystalline Chern FM from stable nodal AFM phase

We now start from the stable nodal phase of $\mathrm{EBR}_{75.5}^{2b}$ ($z_2 = 1$). The breaking of nonsymmorphic TRS unlocks the nodal (Weyl) points which then become free to leave the basal momentum plane (when embedded in 3D). As for the fragile topological phase this results in a fully gapped band structure at $k_z = 0$ where each band acquires a symmetry indicated Chern number given by Eq. (14). Given the band inversion at X between band 2 and 3 required in the fragile to stable topological transition [see the IRREPs ordering in Fig. 3(b)], we now find band Chern numbers

$$\mathcal{C}(1) = \mathcal{C}(2) = \mathcal{C}(3) = \mathcal{C}(4) = +1 \bmod 4. \tag{17}$$

Then, together with the cancellation sum rule $\sum_{i=1}^{4}\mathcal{C}(i) = 0$, we predict $\mathcal{C}(2) = -3$ and $\mathcal{C}(3) = +1$ [or, equivalently, $\mathcal{C}(2) = +1$ and $\mathcal{C}(3) = -3$]. This is confirmed numerically in Fig. 13 of Appendix C. We thus reach the conclusion that for small Zeeman coupling the bands in the vicinity of the half-filling energy must exhibit a higher Chern number. Also, contrary to the gapped FM phase obtained from the fragile topological phase where the valence (conduction) subspace has a trivial summed topology [i.e., $\mathcal{C}(1) + \mathcal{C}(2) = 0$], we here necessarily obtain a nontrivial Chern phase at half-filling with $\mathcal{C}(1) + \mathcal{C}(2) = \pm 2$, thus recovering the general prediction of Eq. (12).

C. Fully pseudo-spin-polarized FM phases

Given the spin-z components associated with the induced IRREPs of the EBR at Γ and M (Table I), we anticipate that by increasing ϵ_{Z} there must be a second transition into a phase with fully pseudo-spin-polarized valence (conduction) bands (right column of Fig. 4), i.e., the $\widetilde{\uparrow}$ ($\widetilde{\downarrow}$) band has a ↑- (↓-) spin component at Γ and M. This phase transition must happen through two band inversions, i.e., at Γ and at M. Assuming $\epsilon_Z > 0$, we infer that beyond the transition the IRREPs ordering at Γ and M are $E(\overline{\Gamma}_7) < E(\overline{\Gamma}_8) < E(\overline{\Gamma}_5) < E(\overline{\Gamma}_6)$, and $E(\overline{M}_5) < E(\overline{M}_6) < E(\overline{M}_8) < E(\overline{M}_7)$, respectively [importantly, note the difference with the ordering of the previous section and Fig. 5(b)]. The question of the Chern numbers, as determined by Eq. (14), is then reduced to the IRREPs ordering at X.

[3] In that case however, there is no spin polarization at Γ and M, which we relate to the fact that 4*d* is not a maximal Wyckoff position for MSG75.1, i.e., the noncolinear in-plane spins at 4*d* can be can superposed on top of each other by moving them to another Wyckoff position with higher symmetry.

First, without loss of generality we can assume that the lowest (highest) energy level has IRREP $\overline{X}_4$ ($\overline{X}_3$), as in Figs. 2(b) and 3(b), from which we get $\mathcal{C}(1) = \mathcal{C}(4) = +1 \bmod 4$. Then, for dominant values of ϵ_Z and λ_{SOC}, we get $\mathcal{C}(2) = \mathcal{C}(3) = -1 \bmod 4$. If we assume intermediary values of ϵ_Z and λ_{SOC} (see below), we instead obtain $\mathcal{C}(2) = \mathcal{C}(3) = +1 \bmod 4$. In the later case [similarly to the discussion below Eq. (17)], one of the two middle bands must exhibit a high Chern number of -3, giving a total Chern number of ± 2 at half-filling for the valence/conduction space.

We now detail the phase transition to the fully polarized phase in the context of the model Eq. (4) to underpin the general scheme outlined above. The fully pseudo-spin-polarized phase must happen through two band inversions, at Γ and M, which are analytically defined for Eq. (4) by the conditions $\epsilon_Z > 2t_3$ and $\epsilon_Z > 2t_2$, respectively (assuming $t_{2,3} > 0$), and with the IRREPs ordering at Γ and M given above for $\epsilon_Z > 0$. The general form of the energy eigenvalues at X for Eq. (4) including the Zeeman term is $\epsilon_{s_1,s_2} = s_1 2t_1 + s_2\sqrt{2|\lambda_2|^2 + \epsilon_Z^2}$ with $s_{1,2} = \pm 1$, and we find $E_\pm(\overline{X}_4) = \epsilon_{-,\pm}$ and $E_\pm(\overline{X}_3) = \epsilon_{+,\pm}$. Fixing $t_1 > 0$, we note that $E_-(\overline{X}_4) \leqslant E_+(\overline{X}_4) \leqslant E_+(\overline{X}_3)$ and $E_-(\overline{X}_4) \leqslant E_-(\overline{X}_3) \leqslant E_+(\overline{X}_3)$. Hence, the lowest and highest energy levels are $E_1 = E_-(\overline{X}_4)$ and $E_4 = E_+(\overline{X}_3)$, respectively, from which we get $\mathcal{C}(1) = \mathcal{C}(4) = 1 \bmod 4$.

The topology of the two remaining bands is then determined by the sign of

$$E_-(\overline{X}_3) - E_+(\overline{X}_4) = 2t_1 - \sqrt{2|\lambda_2|^2 + \epsilon_Z^2}. \tag{18}$$

Let us first we assume $|\lambda_2| > \sqrt{2}t_1$, for which we find $E_2 = E_-(\overline{X}_3) < E_+(\overline{X}_4) = E_3$ for all $\epsilon_Z > 2t_2, 2t_3$, and $\mathcal{C}(2) = \mathcal{C}(3) = -1 \bmod 4$. This case thus has zero Chern number at half-filling.

If we take instead $t_1 > |\lambda_2|/\sqrt{2}$, then either $\epsilon_Z > \sqrt{4t_1^2 - 2|\lambda_2|^2}, 2t_2, 2t_3$, and we reach the same conclusion as before, or $\sqrt{4t_1^2 - 2|\lambda_2|^2} > \epsilon_Z > 2t_2, 2t_3$, in which case $E_2 = E_+(\overline{X}_4) < E_-(\overline{X}_3) = E_3$, and we find $\mathcal{C}(2) = \mathcal{C}(3) = +1 \bmod 4$ which, we have shown, leads to a higher Chern number for band 2 or 3, thus leading to a finite Chern number at half-filling ($\mathcal{C} = 2 \bmod 4$).

We conclude this section by noting that the bands of a single split $\mathrm{EBR}_{75.1}^{2c,\uparrow(\downarrow)}$ must always carry nonzero Chern numbers irrespectively of the ordering of IRREPs.

IV. 3D TOPOLOGY AND GENERAL MSG

Having determined the topology of the 2D projection of MSG75.5 (P_C4) (i.e., for the corresponding magnetic layer group), we now address the 3D topology introducing the third momentum component k_z. First of all, we note that each Kramers doublet at Γ, M, Z, and A, are Weyl points carrying a chirality (Chern number). This results from the chirality of any crystal structure with MSG75.5 (P_C4), see Sec. VI. This nodal topology will be manifested in terms of Fermi arcs on surface spectra only at quarter-filling, and more generally at a filling $\nu \in 2\mathbb{Z} + 1$. In the following, we instead focus on the topology at half-filling, and more generally at a filling $\nu \in 2\mathbb{Z} + 2$.

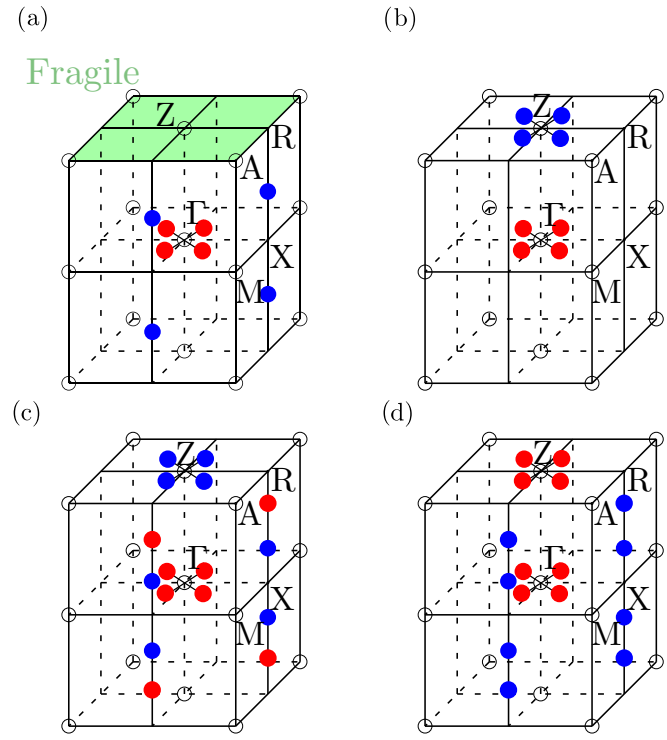

FIG. 6. Topology at half-filling of the 3D $\mathrm{EBR}_{75.5}^{2b}$ for (a) $(z_2^0, z_2^\pi) = (1, 0)$ and (b) (1,1). The colored dots represent the Weyl points (and their chirality) of the crystalline Weyl (CW) phases. The plane with crystalline Euler fragile (CEF) topology is colored in green. TRIM (time reversal invariant) momenta are indicated as open circles. (c) Same as (b) before the annihilation of the Weyl points on the vertical axes. (d) Alternative to (b) when the horizontal (vertical) Weyl points all have equal chirality.

The above results are directly transferable to the $k_z = 0$ and $k_z = \pi$ planes of the 3D Brillouin zone, which leads to a $(z_2^0, z_2^\pi) \in \mathbf{Z}_2^2$ classification. If the two symmetry indicators are distinct, e.g., $(z_2^0, z_2^\pi) = (1, 0)$, they indicate the presence of C_{2z} protected Weyl points (at half-filling) on the $\overline{XR}$ high-symmetry axis, on top of the four Weyl points on the $k_z = 0$ plane, while the plane at $k_z = \pi$ has CEF topology. These thus form a $\mathbf{Z}_2$ indicated octuplet of Weyl points (i.e., the CW topology). It is interesting to note that by C_4 symmetry the Weyl points in plane must all have the same chirality, while the Weyl points on the $\overline{XR}$ axis must all be of the opposite chirality by C_2T symmetry, which leads to the configuration of Fig. 6(a) where the plane with CEF topology is colored in green. If we reverse the indicators, i.e., $(z_2^0, z_2^\pi) = (0, 1)$, the plane with CEF topology moves to $k_z = 0$ and the plane with the Weyl nodes moves to $k_z = \pi$.

When both symmetry indicators are nonzero (obtained from above through a band inversion at R) both planes are stable nodal and we either obtain two quadruplets of Weyl points of opposite chirality in each horizontal plane as illustrated in Fig. 6(b) [after the annihilation on the vertical axes of the nodes with opposite chirality visible in Fig. 6(c)], or we have two octuplets of Weyl points with all Weyl points on the

horizontal planes with the same chirality and all Weyl points on the vertical axes with the opposite chirality as shown in Fig. 6(d).

Only when both symmetry indicators are zero do we retrieve a gapped 3D phase where both planes $k_z = 0$ and $k_z = \pi$ are fragile topological. Our classification thus characterizes and refines the earlier prediction of a $\mathbf{Z}_2$ symmetry indicator for the 3D MSG75.5 (P_C4) phases [35]. As a side remark, we note that planes hosting the four TRIM $\{\Gamma, M, Z, A\}$ characterized by (nonsymmorphic) TRS, i.e., is an antiunitary symmetry squaring to -1 and inverting the momentum, give rise to a nonsymmetry indicated $\mathbf{Z}_2$ index of a strong two-dimensional TI [32]. We note that the nonsymmorphic TRS squares to -1 over the whole plane that contains the four TRIMPs. Therefore, restricting any 3D model on that plane, it can be seen effectively as a 2D system with TRS and the index can be computed in the same way as the Kane-Mele $\mathbf{Z}_2$ invariant [78].

For completeness, let us also mention the axion insulating phases protected by C_2T, i.e., the three-dimensional gapped topological phases indicated by the difference in the second Stiefel Whitney class between the two C_2T symmetric planes $k_z = 0, \pi$ [29,30,42,79]. This phase requires that C_2T squares to $+1$ on both planes and, contrary to its parent phases with inversion symmetry [36], it is not symmetry indicated.

The mechanism discussed so far is directly transferable to the other tetragonal AFM candidate MSG81.37 ($P_C\bar{4}$) and its FM counterpart MSG81.33 ($P\bar{4}$), where the fourfold rotoinversion point symmetry S_4 takes the place of C_4. The only differences with MSG75.5 (P_C4) are the reversal of chirality of the Weyl points under the action of $S_4 = IC_{4z}$ symmetry and, for the 3D gapped phase, the existence of an additional $z_2' \in \mathbf{Z}_2$ symmetry indicator [35] of a strong 3D TI protected by $\mathcal{S}_4$-symmetry and (nonsymmorphic) TRS [80] (see also Appendix D 3 where this symmetry indicator is derived for MSG81.36 ($P_c\bar{4}$) for which it is the unique symmetry indicator of the 3D gapped phase, similarly to MSG81.38 ($P_I\bar{4}$)). The nontrivial value of the symmetry indicator z_2' in Eq. (D4), corresponding to the indicator z_2 identified for MSG81.33 ($P\bar{4}$) in Ref. [36], indicates a 3D axion topological insulating phase with a nontrivial axion angle π [36] and a quantized magnetoelectric response [28,81].

We conclude this section by noting the candidate MSSG77.17 (P_C4_2) that has a $\mathbf{Z}_2$ symmetry indicator [35] which indicates C_2T protected Weyl semimetallic phases, as in MSG75.5 (P_C4), but now with a minimal connectivity of bands of 4, i.e., the filling must be $\nu \in 4\mathbb{Z} + 4$. The 2D gapped phases at $k_z = 0, \pi$ are thus either trivial, or host the second Stiefel Whitney topology that is not symmetry indicated, since the nontrivial Euler class topology only exists within two-band subspaces.

V. COEXISTENCE OF NODAL AND SUBDIMENSIONAL TOPOLOGIES

In the previous MSG candidates we were guided by the possibility of having a nontrivial symmetry indicator of the 3D gapped phase, signaling the possibility of splitting groups of bands (possibly EBRs) into (fragile) topological bands, see also Appendix D. We now address a class of MSGs that host a similar mechanism that nonetheless appear trivial from a standard symmetry indicator or topological quantum chemistry perspective. At the crux of the argument lies the observation that these MSGs host groups of bands (possibly EBRs) that can be split *at planes* in the Brillouin zone, hosting the same (stable) topological features, while their *total* three-dimensional band structure must be connected. Consequently, within these "trivial" groups of bands, i.e., in the sense that they lack 3D symmetry indicators, the in-plane nontrivial signatures must coexist with symmetry indicated nodal structures located away from the (possibly) gapped planes. We discuss below one example where the connectivity of the three-dimensional EBR by itself indicates the presence of protected Weyl points in the direction perpendicular to the 2D topological planes. It thus has stable 3D signatures, such as Fermi arcs [82], which topological origin is independent of the 2D topologies and their signatures. Since the 3D symmetry indicators are blind to this kind of coexistence, these topological phases can thus only be perceived in this refined context of *subdimensional topology*.

We emphasize that our use of subdimensional topology is distinct from the usual correspondence between the topological charges of a d-dimensional node, with codimension δ within a $d + \delta = D$-dimensional Brillouin zone, and the p-dimensional gapped topologies for $\delta - 1 \leqslant p \leqslant D - 1$ [46,83]. The archetypal example of this usual decent approach is the stability of a Weyl point being captured by the Chern number of a gapped sphere surrounding it [84]. We discuss below such as a situation for the case of Weyl nodes protected by the screw axis 4_2 with a chirality $\chi = \pm 2$ captured by gapped Chern planes with $\mathcal{C} = 2 \bmod 4$. Many correspondences of this kind have been formulated recently for new types of crystal-symmetry protected gapped topologies, e.g., Refs. [83,85–87].

In contrast, the new subdimensional topology, we are referring to is independent of the charges of the Weyl nodes protected by the screw symmetry, since we show that the Chern number must be zero on the 2D planes that host the subdimensional topology. This leads to the prediction of new phases with coexisting topological features, i.e., the manifestations of the nodal topology in 3D together with the manifestations of the nontrivial subdimensional topology.

A. Case study of MSG77.18 (P_I4_2)

As an example, we take MSG77.18 (P_I4_2) that hosts the mechanism discussed for MSG75.5 (P_C4) as a 2D subdimensional topology. The coset decomposition of the AFM compatible MSG77.18 (P_I4_2) in terms of its FM partner MSG77.13 ($P4_2$) is $\mathcal{G}_{77.18}/\mathcal{G}_{77.13} = (E|0)\mathcal{G}_{77.13} + (E|\tau_d)'\mathcal{G}_{77.13}$ with $\tau_d = \boldsymbol{a}_1/2 + \boldsymbol{a}_2/2 + \boldsymbol{a}_3/2$, where $\mathbf{T}$ is the primitive Bravais lattice and $\mathcal{G}_{77.13}$ is generated by $(C_{4z}|\tau_3)\mathbf{T}$ with $\tau_3 = \boldsymbol{a}_3/2$. We consider the Wyckoff position (WP) $2a$ [69] that is spanned by the sublattice sites $\boldsymbol{r}_A = \boldsymbol{a}_1/2$ and $\boldsymbol{r}_B = \boldsymbol{a}_2/2 + \boldsymbol{a}_3/2$. The same sites correspond to WP $2c$ of MSG77.13. Populating the sites with s-electronic orbitals and both spin-z-1/2 components we get the Bloch orbital basis $|\boldsymbol{\varphi}, \boldsymbol{k}\rangle$ with $\boldsymbol{\varphi} = (\varphi_{A\uparrow}, \varphi_{A\downarrow}, \varphi_{B\uparrow}, \varphi_{B\downarrow})$ forming an elementary band representation which we write $\mathrm{EBR}^{2a}_{77.18}$. $\mathrm{EBR}^{2a}_{77.18}$

resembles $\mathrm{EBR}^{2b}_{75.5}$ except that it is *indecomposable* over the 3D Brillouin zone.

An other important difference with MSG75.5 (P_C4) is the algebra of symmetries at $k_z = \pi$. Taking a point on the $k_z = \pi$ plane $\bar{\boldsymbol{k}} = (k_x, k_y, \pi)$, the C_2T symmetry in MSG77.18 (P_I4_2) is represented for $\mathrm{EBR}^{2a}_{77.18}$ by

$$\begin{aligned}\langle \boldsymbol{\varphi}, \bar{\boldsymbol{k}}|^{(C_{2z}|\tau_d)'}|\boldsymbol{\varphi}, \bar{\boldsymbol{k}}\rangle &= \mathrm{e}^{\mathrm{i}\boldsymbol{k}C_{2z}\tau_d}\langle \boldsymbol{\varphi}, \bar{\boldsymbol{k}}|\boldsymbol{\varphi}, IC_{2z}\bar{\boldsymbol{k}}\rangle(\sigma_x \otimes \mathrm{i}\sigma_x)\mathcal{K} \\ &= \mathrm{e}^{\mathrm{i}\boldsymbol{k}C_{2z}\tau_d}\langle \boldsymbol{\varphi}, \bar{\boldsymbol{k}}|\boldsymbol{\varphi}, \bar{\boldsymbol{k}} - \boldsymbol{b}_3\rangle(\sigma_x \otimes \mathrm{i}\sigma_x)\mathcal{K} \\ &= \mathrm{e}^{\mathrm{i}\boldsymbol{k}C_{2z}\tau_d}\hat{T}(-\boldsymbol{b}_3)(\sigma_x \otimes \mathrm{i}\sigma_x)\mathcal{K}, \end{aligned} \tag{19}$$

with $\hat{T}(-\boldsymbol{b}_3) = \mathrm{diag}(\mathrm{e}^{\mathrm{i}\boldsymbol{r}_A\cdot\boldsymbol{K}}, \mathrm{e}^{\mathrm{i}\boldsymbol{r}_A\cdot\boldsymbol{K}}, \mathrm{e}^{\mathrm{i}\boldsymbol{r}_B\cdot\boldsymbol{K}}, \mathrm{e}^{\mathrm{i}\boldsymbol{r}_B\cdot\boldsymbol{K}})_{\boldsymbol{K}=-\boldsymbol{b}_3} = \mathrm{diag}(1, 1, -1, -1)$. We thus find the square to be $\langle \boldsymbol{\varphi}, \bar{\boldsymbol{k}}|^{[(C_{2z}|\tau_d)']^2}|\boldsymbol{\varphi}, \bar{\boldsymbol{k}}\rangle = -\mathbb{1}_{4\times4}$, i.e., the C_2T symmetry squares to -1. The bands hence exhibit a twofold Kramers degeneracy over the whole $k_z = \pi$ plane

1. Model and band structure

We illustrate this with the following minimal 3D extension of Eq. (4) which we rewrite as $H[f_1, f_2, f_3, g_1, g_2](\boldsymbol{k})$,

$$\begin{aligned}H'(\boldsymbol{k}) &= H[f_1, f_2', f_3', g_1, g_2'](\boldsymbol{k}) \\ &\quad + \rho_1 h_1(\boldsymbol{k})\sigma_x \otimes \sigma_z + \rho_2 h_2(\boldsymbol{k})\sigma_y \otimes \sigma_z, \end{aligned} \tag{20}$$

where the new lattice form factors are now extended to 3D momentum space,

$$\begin{aligned} f_2'(\boldsymbol{k}) &= (\cos\boldsymbol{\delta}_1'\boldsymbol{k} - \cos\boldsymbol{\delta}_2'\boldsymbol{k} + \cos\boldsymbol{\delta}_3'\boldsymbol{k} - \cos\boldsymbol{\delta}_4'\boldsymbol{k})/2, \\ f_3'(\boldsymbol{k}) &= (\cos\boldsymbol{\delta}_1'\boldsymbol{k} + \cos\boldsymbol{\delta}_2'\boldsymbol{k} + \cos\boldsymbol{\delta}_3'\boldsymbol{k} + \cos\boldsymbol{\delta}_4'\boldsymbol{k})/2, \\ g_2'(\boldsymbol{k}) &= (\sin\boldsymbol{\delta}_1'\boldsymbol{k} - \mathrm{i}\sin\boldsymbol{\delta}_2'\boldsymbol{k} - \sin\boldsymbol{\delta}_3'\boldsymbol{k} + \mathrm{i}\sin\boldsymbol{\delta}_4'\boldsymbol{k})/2, \\ h_1(\boldsymbol{k}) &= (\sin\boldsymbol{\delta}_1'\boldsymbol{k} + \sin\boldsymbol{\delta}_2'\boldsymbol{k} + \sin\boldsymbol{\delta}_3'\boldsymbol{k} + \sin\boldsymbol{\delta}_4'\boldsymbol{k})/2, \\ h_2(\boldsymbol{k}) &= (\sin\boldsymbol{\delta}_1'\boldsymbol{k} - \sin\boldsymbol{\delta}_2'\boldsymbol{k} + \sin\boldsymbol{\delta}_3'\boldsymbol{k} - \sin\boldsymbol{\delta}_4'\boldsymbol{k})/2, \end{aligned} \tag{21}$$

with $\boldsymbol{\delta}_{1,2}' = \boldsymbol{\delta}_{1,2} + \boldsymbol{a}_3/2$, and $\boldsymbol{\delta}_{3,4}' = -\boldsymbol{\delta}_{1,2} + \boldsymbol{a}_3/2$, and with the new real parameters $\rho_1, \rho_2 \in \mathbb{R}$ (we take $\rho_1 = -1$ and $\rho_2 = -2/5$).

We show the band structure of model Eq. (20) in Fig. 7(a) where the k_z-axis covers $[0, 2\pi]$, and the other axis corresponds to the successive paths ΓX and XM within the plane $k_z = 0$. The band structure along the high-symmetry lines is shown in Figs. 8(a) and 8(c) after a band inversion at X. We note the twofold degeneracy at $k_z = \pi$ which explains the degeneracies along $\overline{\mathrm{ZR}}$ and $\overline{\mathrm{RA}}$ in Figs. 7(a), 8(a), and 8(c).

Importantly, the compatibility relations along the C_4-symmetric axes $\overline{\Gamma Z}$ and $\overline{MA}$ imply that the EBR cannot be split [69], see Appendix D 2. Indeed, the fourfold screw symmetry $4_2 \equiv (C_{4z}|\tau_3)$ imposes an exchange of branches between the Kramers doublets of Γ and Z (M and A), see the coIRREPs given in Table II retrieved from [69]. This leads to two 4_2-protected nodal points on the $\overline{\Gamma Z}$ line (respectively, the $\overline{MA}$ line) at half-filling [marked by circles in Fig. 7(a)], and more generally at a filling $\nu \in 4\mathbb{Z} + 2$. We note that this exchange of IRREPs along the 4_2-axes originates from the monodromy of the irreducible representations of the screw symmetry 4_2 [6,66,69,83,88].

2. Chirality of Weyl nodes protected by a screw axis 4_2

Following the algebraic argument of Ref. [6], see also Ref. [83], we now derive the symmetry enforced chirality

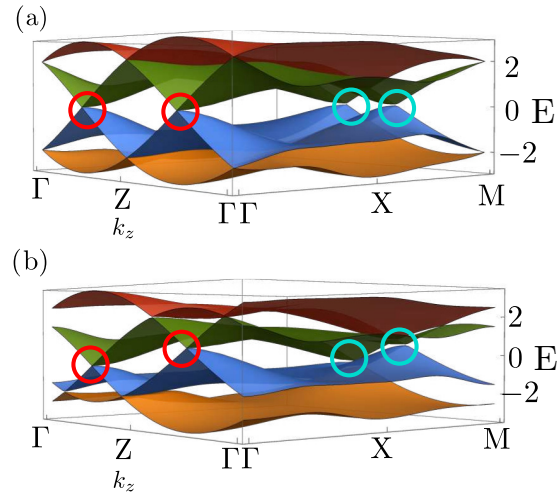

FIG. 7. Subdimensional gapped phases within a 3D indecomposable EBR, illustrated by (a) $\mathrm{EBR}^{2a}_{77.18}$ and (b) $\mathrm{EBR}^{2c}_{77.13}$ obtained by breaking TRS through a Zeeman coupling. The Weyl nodes imposed at half-filling by the screw axis 4_2 are marked with colored circles indicating the sign of the symmetry-imposed chiralities.

of $\chi = 2 \bmod 4$ for each Weyl point protected by 4_2. Let us start with a sphere $\mathbb{S}$ surrounding one of the Weyl points, say the one on the upper half of the $\overline{\Gamma Z}$ line. We fix the south pole at Γ and the north pole at Z, see Fig. 9(a). Then, we divide the sphere in four quarters, one of which, let us call it $\mathcal{S}$, is bounded by an oriented loop $\partial S \equiv l = l_b \circ l_a$ (which we read as first l_a followed by l_b) with $l_a = C_{4z}l_b^{-1}$ (where l_b^{-1} is the reversed oriented path), see Fig. 9(a). Since we can recompose the total sphere through C_{4z} actions, i.e., $\mathbb{S} = \mathcal{S} \cup C_{4z}\mathcal{S} \cup C_{4z}^2\mathcal{S} \cup C_{4z}^3\mathcal{S}$, the Chern number of the two occupied bands over the gapped sphere thus reads

$$\mathrm{e}^{-\mathrm{i}2\pi\mathcal{C}[S]} = (\mathrm{e}^{-\mathrm{i}\gamma_B[l]})^4 = \mathrm{e}^{-\mathrm{i}4\gamma_B[l]}, \tag{22}$$

by the invariance of the Berry curvature under rotation symmetry [6], and where $\gamma_B[l]$ is the Berry phase of the two occupied bands over the loop $l = l_b \circ l_a$, i.e., (see the definition of symmetry transformation of the Wilson loop in Appendix A)

$$\begin{aligned}\mathrm{e}^{-\mathrm{i}\gamma_B[l]} &= \det\mathcal{W}[l] = \det(\mathcal{W}[l_b]\cdot\mathcal{W}[l_a]) \\ &= \det\left(R^{\Gamma}_{4_2}\cdot\mathcal{W}[l_a]^{-1}\cdot\left(R^{Z}_{4_2}\right)^{-1}\cdot\mathcal{W}[l_a]\right) \\ &= \det\left(R^{\Gamma}_{4_2}\cdot\left(R^{Z}_{4}\right)^{-1}\right) = \frac{\chi_{4_2}(\overline{\Gamma}_5)\chi_{4_2}(\overline{\Gamma}_7)}{\mathrm{i}\chi_{4_2}(\overline{Z}_5)\mathrm{i}\chi_{4_2}(\overline{Z}_8)} \\ &= (-\mathrm{i})^2 = -1, \end{aligned} \tag{23}$$

where $R^{\Gamma}_{4_2} = \mathrm{e}^{\mathrm{i}C_{4z}\boldsymbol{k}_\Gamma\cdot\tau_3}S^{\Gamma}_{4_2}(\overline{\Gamma}_i\overline{\Gamma}_j) = S^{\Gamma}_{4_2}(\overline{\Gamma}_i\overline{\Gamma}_j)$ and $R^{Z}_{4_2} = \mathrm{e}^{\mathrm{i}C_{4z}\boldsymbol{k}_Z\cdot\tau_3}S^{Z}_{4_2}(\overline{Z}_i\overline{Z}_j) = \mathrm{i}S^{Z}_{4_2}$ $(C_{4z}\boldsymbol{k}_Z\cdot\tau_3 = \boldsymbol{b}_3/2\cdot\boldsymbol{a}_3/2 = \pi/2)$ are defined in terms of the representation of symmetry $(g|\tau_g)$ in the valence band basis $S^{\boldsymbol{k}}_{(g|\tau_g)}(\bar{\boldsymbol{k}}_i\bar{\boldsymbol{k}}_j)$ for a coIRREP $\bar{\boldsymbol{k}}_i\bar{\boldsymbol{k}}_j$ at a momentum $\boldsymbol{k}$, and $\chi_4(\bar{\boldsymbol{k}}_i)$ is the character of the IRREP $\bar{\boldsymbol{k}}_i$ given in Table I (we have $\chi_4(\overline{Z}_i) = \chi_4(\overline{\Gamma}_i)$ [69]). Therefore $\gamma_B[l] = \pi \bmod 2\pi$ and we conclude that the Chern number over the whole sphere, and thus the chirality of the Weyl point inside, is $\mathcal{C}[\mathbb{S}] = 2 \bmod 4$. Very interestingly, we find

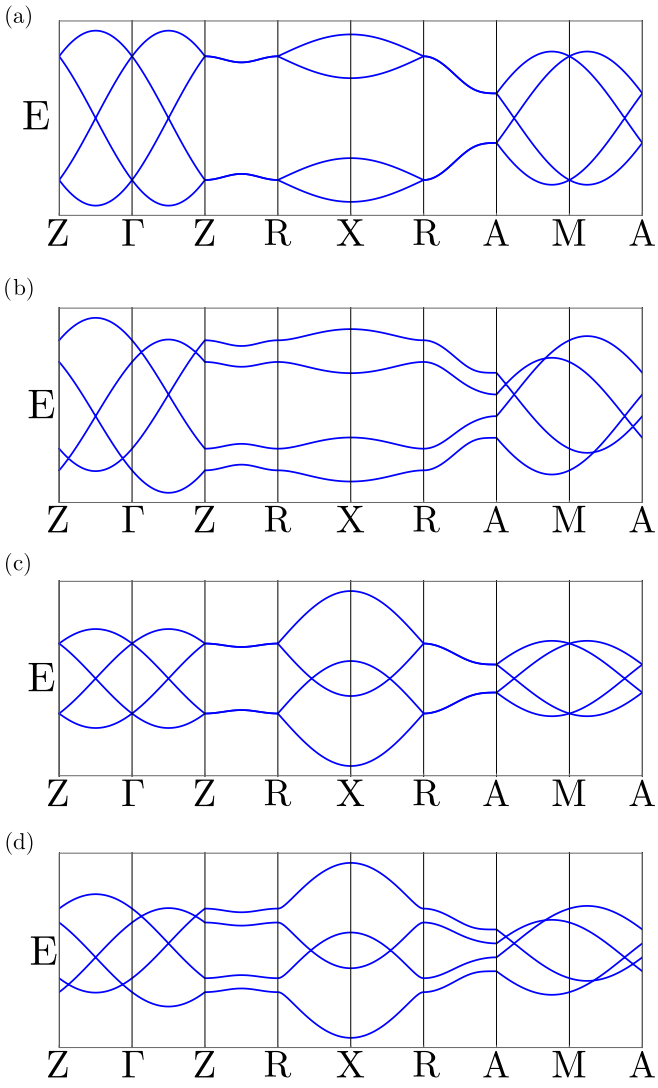

FIG. 8. Band structure along high-symmetry lines for $\mathrm{EBR}^{2a}_{77.18}$ (a) with $z_2^0 = 0$ and (c) with $z_2^0 = 1$, and for $\mathrm{EBR}^{2c}_{77.13}$ obtained through Zeeman splitting (b) from (a) and (d) from (c).

a quadratic dispersion in the (k_x, k_y)-plane at a fixed k_z from each Weyl point at half-filling in Fig. 7, see also [88].

While the above derivation based on the symmetry reduction of Wilson loop, first developed in Refs. [6,83] adapting the Wilson loop techniques developed eariler to assess gapped topological phases in Refs. [13,77,89–91], is completely general and can be readily transferred to any other context (i.e., any other space group, with or without spin-orbit coupling), we note some later alternative approaches in Ref. [88,92].

3. AFM topological phases

We now discuss the global topology of the AFM topological phases for MSG77.18 (P_I4_2). We first note that $\mathrm{EBR}^{2a}_{77.18}$ can be gapped over the planes $k_z = 0, \pi$. The 2D topology at $k_z = 0$ for $\mathrm{EBR}^{2a}_{77.18}$ is the same as the topology discussed for $\mathrm{EBR}^{2b}_{75.5}$, that is CEF topology versus stable nodal (CW topology) indicated by z_2 in Eq. (10). We therefore can define a subdimensional $z_2^0 \in \mathbf{Z}_2$ symmetry indicator. We have seen that on the $k_z = \pi$ plane the C_2T symmetry squares to -1,

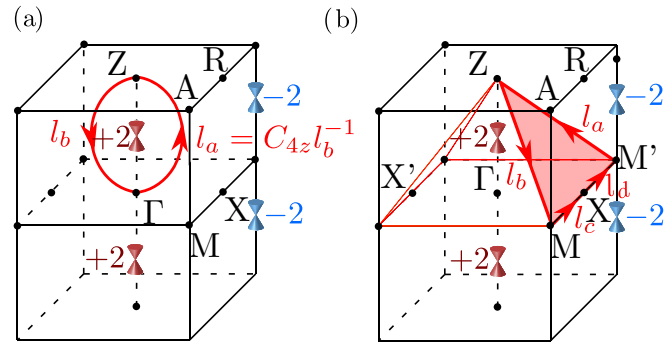

FIG. 9. Chirality of $\chi = 2 \bmod 4$ for each Weyl point protected by the 4_2 screw axis on the $\overline{\Gamma Z}$ and $\overline{MA}$ lines, at half-filling ($\nu \in 4\mathbb{Z} + 2$), derived from the symmetry reduction of the Wilson loop (see text).

such that there is no (real) Euler class topology. Nevertheless, we show in Fig. 10 the C_4-symmetric Wilson loop on the plane $k_z = \pi$ for the model for MSG77.18 (P_I4_2) Eq. (20), over (a) the conduction and (b) valence bands. The winding of Wilson loop for the conduction bands indicates a crystalline (non-Euler) fragile (CF) topology.

We now determine how the subdimensional topologies (at $k_z = 0, \pi$) interact with the topology of the 4_2-symmetry protected Weyl points. We first note that the Chern number at half-filling vanishes on the $k_z = 0, \pi$-planes as a consequence of C_2T symmetry (see the discussion below Eq. (11) for $k_z = 0$, and at $k_z = \pi$, we have $\mathcal{F} \equiv 0$ by $[C_2T]^2 = -1$). As a consequence, we can deform the sphere $\mathbb{S}$ of Fig. 11(a) into the pyramid $\mathbb{P}$ of Fig. 11(b), while conserving the Chern number, i.e., $\mathcal{C}[\mathbb{S}] = \mathcal{C}[\mathbb{P}] = 2 \bmod 4$. This equality can be readily verified through the symmetry reduction of the Wilson loop $\mathcal{W}[l_d \circ l_c \circ l_b \circ l_a]$ similarly to the above derivation for $\mathbb{S}$ but now using both C_{4z} and C_{2z} transformations [6]. We note that even if there are nodal points on the $k_z = 0$ plane (for $z_2 = 1$), by C_4 symmetry they must contribute to an increase of the Chern number by ± 4, which leaves the quantity mod 4 unchanged. An other consequence of C_2T symmetry is that any Weyl point above the $k_z = 0$ plane must have its mirror symmetric image underneath ($k_z \to IC_{2z}k_z = -k_z$) with the same chiral charge. Combining the top of the pyramid in Fig. 9(b) with its mirror image in the k_z direction, we obtain an octahedron $\mathbb{O} = \mathbb{P} \cup m_z\mathbb{P}$ that wraps the pair of Weyl points on the $\overline{\Gamma Z}$ line, and over which there is a total Chern number (chirality) of $\mathcal{C}[\mathbb{O}] = (2 + 2) \bmod 8 = 4 \bmod 8$.

We note that $\mathbb{O}$ divides the 3D Brillouin zone in two symmetric halves. Invoking the Nielsen-Ninomiya cancellation

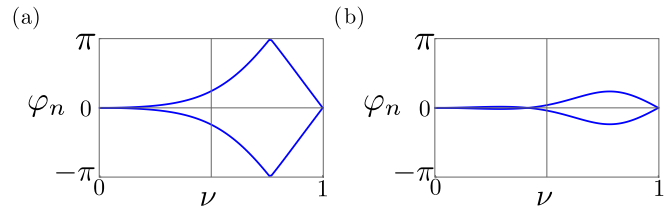

FIG. 10. C_4-symmetry Wilson loop for the conduction (a) and valence (b) bands of $\mathrm{EBR}^{2a}_{77.18}$ at $k_z = \pi$.

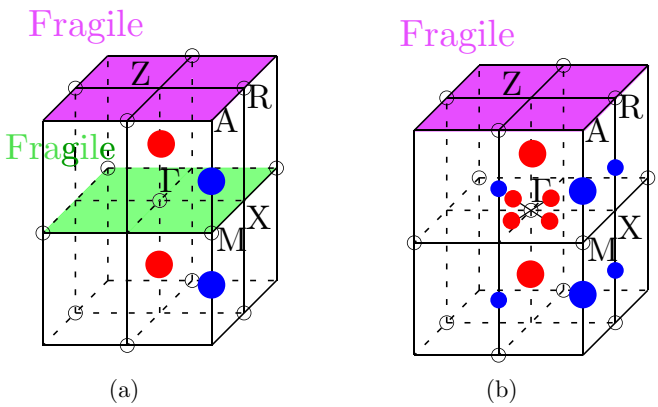

FIG. 11. Topology at half-filling of the 3D $\mathrm{EBR}^{2a}_{77.18}$ for (a) $z_2^0 = 0$ and (b) 1. The colored dots represent the Weyl points and their chirality, with $\chi = \pm 1$ for the small dots, and $\chi = \pm 2$ for the big dots, of the crystalline Weyl (CW) phases. The double Weyl points on the vertical axes are protected by the screw 4_2 symmetry, see Sec. V A 2. The plane with crystalline Euler fragile (CEF) topology is colored in green, and the plane with (C_4-symmetry protected) crystalline fragile (CF) topology is colored in purple. TRIM (time reversal invariant) momenta are indicated as open circles.

theorem [93], it follows that the total chirality inside $\mathbb{O}$ (say $+4$), must be compensated by the total chirality inside the complement of $\mathbb{O}$ (-4), see Fig. 9. We then arrive for $z_2 = 0$ to the configuration of Fig. 11(a), where the green (purple) plane hosts a CEF (CF) topology, and where each red (blue) point mark a Weyl point with $\chi = +2$ (rep. $\chi = -2$). We finally conclude that this phase must exhibit large double Fermi arcs in the surface spectra connecting pairs of projected Weyl nodes of opposite chirality across the surface Brillouin zone. Also, by inverting IRREPs at X, i.e., setting $z_2^0 = 1$, we get the octuplet of Weyl points discussed above in the 3D phase of MSG75.5 (P_C4), leading to the configuration of Fig. 11(b). This last case must exhibit an exotic coexistence of Fermi arcs generated by different sets of Weyl points with qualitatively distinct topological origins.

Our subdimensional analysis has thus allowed us to identify new phases with the coexistence of 2D and 3D nodal topological features.

4. AFM-FM correspondence

We now consider the effect of breaking the nonsymmorphic TRS, i.e., inducing a transition from the AFM phase of MSG77.18 (P_I4_2) to the FM phase of MSG77.13 ($P4_2$). This can be done by including a Zeeman splitting as we did for MSG75. We show the band structure in Figs. 7(b), and along the high-symmetry lines in Figs. 8(b) and 8(d) after a band inversion at X. We find that all the Kramers degeneracies are split leaving gapped bands on the $k_z = 0$ and π planes. Similarly to the case of MSG75.1 ($P4$), the topology of the gapped bands at fixed k_z are characterized through symmetry indicated Chern numbers (i.e., with CC topology). Interestingly, for moderate Zeeman coupling, the four bands remain fully connected along the C_4-symmetric axes through the persistence of the C_4-symmetry protected Weyl nodes, as indicated by the IRREP order at Γ, Z, M, and A, as it is clearly shown in Figs. 8(b) and 8(d).

We note however that, by relaxing the pairing conditions (i.e., from 2D coIRREPs to 1D IRREPs), there are more combinatorial ways of connecting the bands allowed by the compatibility relations for MSG77.13 ($P4_2$). In particular, the bands can be ordered at $\{\Gamma, Z, M, A\}$ as to avoid Weyl points at half-filling (more generally at a filling $\nu \in 4\mathbb{Z} + 2$).

5. Stable 3D signatures

We emphasize that the rational of subdimensional topologies thus works in two manners. Firstly, because the total 3D EBR is connected, and thus trivial, these phases are missed by previous schemes. Reciprocally, the presence of in plane topology together with the nodes to make the EBR globally connected implies the coexistence of topological signatures of qualitatively distinct origins. On one hand, the connectivity condition directly induces symmetry indicated Weyl points, and in turn, Fermi arcs in the surface spectra. On the other hand, the subdimensional topology is either gapless, in which case it induces additional Weyl points and thus additional Fermi arcs, or it is gapped fragile topological, in which case it induces corner modes [56]. In this sense, this mechanism can thus be used to find new topological signatures that are directly detectable via the usual routes of, e.g., angle resolved photoemission spectroscopy, quantum oscillation techniques or scanning tunneling microscopy.

B. Generalization

We end by generalizing our subdimensional topology scheme and search systematically for candidate MSGs hosting the planar topologies discussed so far—that is, CEF, CF, and CW phases for the AFM cases and CC phases for their FM counterpart—and the outlined mechanisms relating them. Remarkably, our results are directly transferable to all tetragonal MSGs with the point groups C_4 and S_4, i.e., comprising space group families SG75-SG82. For each family we then consider all the Shubnikov type IV AFM MSGs and the one type I FM MSG. This amounts to a total of 26 MSGs which we list in Table III, where we give the type of planar topologies for $k_z = 0$ and $k_z = \pi$, and the list of EBRs hosting these. On top of the single EBRs that split on both planes, $k_z = 0$ and $k_z = \pi$, and which *must* necessarily host a nontrivial planar topology of type indicated, we have also listed the sums of EBRs that *can* lead to a listed topology upon the permutation of their IRREPs. Whenever there is the choice CEF/CW, the topology is determined by the ordering of IRREPs. We note that $[C_2T]^2 = \pm 1$ indicates CEF or CEF/CW ($+1$) versus CF (-1) topology [4][94] as the only alternative since the Chern number must vanish. Finally, all FM candidates acquire CC topology when obtained from their AFM parents through Zeeman splitting. In particular, every nodal AFM phase at half-filling must give rise to a nontrivial Chern FM phase at half-filling, thus constituting a systematic correspondence

[4]In case of CEF, the quantization of the Wilson loop over the base path $\Gamma X \Gamma'$ follows either from the condition that $\xi_2^\Gamma(1) = \xi_2^\Gamma(2)$ [equivalently, $\xi_2^M(1) = \xi_2^M(2)$], or if both Γ and X are TRIMs in which case the Wilson loop phases are also Kramers degenerate at $\{0, 0\}$ or $\{\pi, \pi\}$.

between necessarily nontrivial topological phases associated to MSG representations.

VI. CHIRAL FERMIONS AT HIGH-SYMMETRY MOMENTA AND LARGE FERMI ARCS

All the MSGs of the table with point group C_4 (i.e., the type IV AFM MSG75.4-MSG81.36, and the type I FM MSG75.1-MSG80.29) have only proper symmetries, a consequence of which is that any crystal structure that explicitly breaks all symmetries not included in their MSG must be chiral, i.e., enantiomorphic (the SGs 75-76-77-78-79-80 are all among the 65 Sohncke space groups with no inversion, no mirror, nor rotoinversion symmetries [95]). Then, the absence of improper symmetry allows the existence of Weyl nodes at high-symmetry momenta, i.e., with nonvanishing Chern numbers. This is the rationale for the chiral Fermions found in many (nonmagnetic) material candidates with a Sohncke space group [6,96–100].

We have noted that MSG75.5 (P_C4) and MSG77.18 (P_I4_2) exhibit Weyl nodes at every TRIMP at a filling $2\mathbb{Z}+1$. MSG77.18 must also exhibit Weyl nodes on the $\overline{\Gamma Z}$- and $\overline{MA}$-lines at a filling $4\mathbb{Z}+2$ due to the monodromy of the irreducible representation of the screw axis 4_2. The same results apply to the FM parents MSG75.1 ($P4$) and MSG77.13 ($P4_2$). The Weyl points at high-symmetry momenta for all the other MSGs of the table can be found similarly.

In Ref. [6], we have given a detailed analysis of the symmetry indicated higher Chern number generated by the Weyl points locked on a screw axis at half-filling, and derived the necessary existence of large Fermi arcs due to the compensation of chirality across the Brillouin zone. This analysis can be readily transferred to the present situation (e.g., here $\mathcal{C}=\pm 2$ on the 4_2-axes). Large Fermi arcs has also been reported in other nonmagnetic chiral materials [97,98].

In the next section, we discuss the fate of the Weyl points when extra improper point symmetries are included.

We now turn to the MSGs with rotoinversion symmetry IC_{4z}. Since the chirality of Weyl points is reversed under IC_{4z}, the Kramer's degeneracies at the TRIMPs (which are also IC_{4z} invariant momenta) cannot form Weyl nodes at the filling $2\mathbb{Z}+1$. Instead, each double degeneracy at a TRIMP on the $k_z=0$ plane is continued as a nodal line for all values of k_z [69].

VII. RAISING AND LOWERING OF SYMMETRIES

So far, we have focused on the topological correspondence between representations of magnetic space groups with the tetragonal point groups C_4 and S_4. We now briefly address the effect of adding and removing unitary symmetries.

A. Magnetic Dirac fermions

Let us start by including extra unitary symmetries to MSSG75.5 (P_C4). If we include one extra vertical mirror symmetry, say m_y, the MSG is promoted to MSG99.169 (P_C4mm) with the (unitary) point group C_{4v} ($4mm$). Remarkably the four bands become all connected through a fourfold magnetic Dirac node at M, similarly to the examples discussed in Ref. [55].

The same happens for MSG89.93 (P_C422), obtained by including one horizontal π-rotation symmetry (say C_{2y}) leading to the point group D_4 (422), as well as for MSG83.49 (P_C4/m), obtained by including the basal mirror symmetry m_z leading to the point group C_{4h} ($4/m$).

The structural chirality is lost for MSG99.169 (P_C4mm) and MSG83.49 (P_C4/m), thus preventing the existence of Weyl nodes at the TRIMPs, i.e., the Weyl points are absorbed within vertical nodal lines on the C_{4z}-axes, and, respectively, within a global twofold Kramer's degeneracy. For MSG89.93 (P_C422) instead, the structural chirality, and thus the Weyl nodes, are preserved.

We note that the introduction m_z allows the definition of C_4-symmetry indicated mirror Chern numbers [13,80,101]. The systematic study of the magnetic topological phases for the next magnetic superspace groups, however, lies beyond the scope of the present work.

B. Weyl phases protected by $[C_2T]^2=+1$

The symmetry indicator Eq. (10) and its interpretation in terms of a $\mathbb{Z}_2$ quantized Berry phase Eq. (11), derived here for MSG75.5 (P_C4), can be readily applied to many other MSGs with gapped 2D planes in the Brillouin zone where $[C_2T]^2=+1$. The simplest example MSG3.4 (P_a2), obtained by forgetting the C_4 symmetry, has a $\mathbb{Z}_2$ symmetry indicator that readily corresponds to z_2 Eq. (10) [35]. For many MSGs though, there are symmetry indicated nodal points between the gapped planes, i.e., similarly to MSG77.18 (P_I4_2), such that they cannot be identified by a (3D) symmetry indicator and they have been listed as trivial [35].

C. Chern and Weyl phases of type I MSGs

We have discussed in detail the transition from the AFM Weyl phase of MSG75.5 (P_C4), and MSG77.18 (P_I4_2), to the subdimensional Chern insulating FM phases of MSG75.1 ($P4$), and MSG77.13 ($P4_2$), respectively, obtained upon the breaking of the nonsymmorphic TRS. The effect of breaking TRS is to unlock the Weyl nodes that were pinned on the C_2T planes, so that they move within the Brillouin zone. We conclude that the symmetry indicator $\mathbb{Z}_4$ of the type I MSG75.1 ($P4$) [35] indicates a Weyl semimetallic phase, while there is no symmetry indicator for MSG77.13 ($P4_2$) [35] with a Weyl semimetallic phase that must be assessed in terms of subdimensional topology.

In the same way as we predict many AFM phases with C_2T protected Weyl nodal phases, we predict many FM Weyl nodal phases indicated by subdimensional Chern phases upon the breaking of the nonsymmorphic TRS.

VIII. CONCLUSIONS

In conclusion, starting from the specific case study, MSG 75.5 (P_C4), we find that specific Wyckoff positions ($2b$) in this magnetic ground group necessarily results in (fragile) topological bands. In this regard we formulated a first generic model exhibiting fragile topology in the context of magnetic space group symmetries. Breaking the essential symmetry by a Zeeman term then relates the underlying AFM-compatible MSG with a FM counterpart in the same space group

family and ensures that the fragile topology gaps into bands with finite Chern number. After translating the $\mathbf{Z}_2$ symmetry indicator of the AFM MSG into a quantized Berry phase of a stable topological semimetallic phase, which originates from the combination of C_4 symmetry and C_2T-protected Euler class topology, we also discuss a similar correspondence to FM Chern phases. We thus unveil a systematic correspondence between necessarily nontrivial topological phases associated with MSG representations. Moreover, we then promote this mechanism to three spatial dimensions, where we also find novel phases characterized by the concept of *subdimensional topologies*. The latter feature the same in-plane mechanism but have 3D elementary band representations that are fully connected. As a result, the nontrivial 2D topology must coexists with nodes away from the high-symmetry planes, e.g., Weyl points, giving rise to additional topological nodal features, such as Fermi arcs, that can be diagnosed with established experimental methods. As a result, our work culminates in an exhaustive list of tetragonal MSGs (with the point groups C_4 and S_4) and their EBR content hosting the above correspondence. We have then addressed the effect of adding and removing unitary symmetries that lead to the identification of magnetic Dirac (fourfold) points, and have outlined how the symmetry indicated Weyl semi-metallic phases protected by C_2T can be found in numerous MSGs as a result of our refined subdimensional topological analysis. Given the generality of these insights and relevance of parameters to access this physics, we hope our results pave the way for new pursuits in topological band structures. In fact, we anticipate that this coexistence effect, i.e., of gapped subdimensional topology together with independent topological nodes, can also occur in the nonmagnetic context culminating in novel gapped-nodal topological phases.

Note added. We finally note that our results agree with expressions for magnetic EBRs, compatibility relations and symmetry indicators tabulated in Ref. [36], which was posted during the finalizing stages of this manuscript. We comment here on Ref. [101] that appeared recently and has some overlap with our work. Among many results not covered by our work, they give a complete list of MSGs that have z_2 (called z_4 in their work) as one of the 3D symmetry indicators, including some of the MSGs discussed here. While the scope of our work was more restricted, our approach based on subdimensional topologies, i.e., allowing symmetry indicated nodes between gapped planes, leads us to predict many more MSGs with C_2T protected Weyl semi-metallic phases. Ref. [101] also considers other Weyl semi-metallic phases in type I MSGs protected by IC_{4z} symmetry, among which are MSG81.33 ($P\bar{4}$) and MSG82.39 ($P\bar{4}$). Alternatively, these FM phases can be readily obtained, upon the breaking of the nonsymmorphic TRS, from the (subdimensional) AFM Weyl phases of the following type IV MSG81.36 ($P_c\bar{4}$), MSG81.37 ($P_C\bar{4}$), MSG81.38 ($P_I\bar{4}$), and MSG82.42 ($I_c\bar{4}$), all listed in our table.

ACKNOWLEDGMENTS

R.-J. S. acknowledges funding from the Marie Skłodowska -Curie programme under EC Grant No. 842901 and the Winton programme as well as Trinity College at the University of Cambridge. G.F.L acknowledges funding from the Aker Scholarship.

APPENDIX A: WILSON LOOP WINDING FOR THE FRAGILE TOPOLOGICAL PHASE

We algebraically derive the symmetry obstruction on the winding of Wilson loop over one quarter of the Brillouin zone, and following over the whole Brillouin zone, for the valence (conduction) subspace of the split $\mathrm{EBR}^{2b}_{75.5}$. For this we choose the patch of the Brillouin zone bounded by $l_{\Gamma X\Gamma'}$ and $l_{\Gamma M\Gamma'}$, see Fig. 2(c) (blue dashed). We design a flow starting with the base path $l_{\Gamma X\Gamma'}$ and ending with $l_{\Gamma M\Gamma'}$. Defining the Wilson loop phases

$$\{\varphi_1, \varphi_2\} = \mathrm{Arg}[\mathrm{eig}\{\mathcal{W}[l_{\Gamma X\Gamma'}]\}],$$
$$\{\varphi_1', \varphi_2'\} = \mathrm{Arg}[\mathrm{eig}\{\mathcal{W}[l_{\Gamma M\Gamma'}]\}], \tag{A1}$$

they must extrapolate smoothly between $\{\varphi_1, \varphi_2\}$ and $\{\varphi_1', \varphi_2'\}$ as we smoothly deform the base path from $l_{\Gamma X\Gamma'}$ to $l_{\Gamma M\Gamma'}$. The Wilson loop over an oriented base path $l : k_1 \to k_2$ is defined through $\mathcal{W}_{k_2\leftarrow k_1} = \langle \boldsymbol{u}, k_2|\hat{W}|\boldsymbol{u}, k_1\rangle$ where $|\boldsymbol{u}, k_1\rangle$ is the matrix of Bloch eigenvectors of the band subspace under consideration, and $\hat{W} = \prod_k^{k_2\leftarrow k_1} \mathcal{P}(k)$ with the projector $\mathcal{P}(k) = |\boldsymbol{u}, k\rangle\langle \boldsymbol{u}, k|$.

We now show that the crystal symmetries act as an obstruction imposing the quantization of Wilson loop phases. First, we find

$$\mathcal{W}[l_{\Gamma X\Gamma'}] = \mathcal{W}_{\Gamma'\leftarrow X} \cdot \mathcal{W}_{X\leftarrow\Gamma}$$
$$= R_2^{\Gamma} \cdot \mathcal{W}^{-1}_{X\leftarrow\Gamma} \cdot \left(R_2^{X}\right)^{-1} \cdot \mathcal{W}_{X\leftarrow\Gamma}, \tag{A2}$$

where $R_2^{\bar{\boldsymbol{k}}} = \langle \boldsymbol{u}, D_\pi\bar{\boldsymbol{k}}|\hat{U}(C_{2z})|\boldsymbol{u}, \bar{\boldsymbol{k}}\rangle$ is the sewing matrix of symmetry C_{2z} at the high-symmetry point $\bar{\boldsymbol{k}}$ in the valence Bloch eigenvectors basis (with $\hat{U}(C_{2z}) = \mathbb{1} \otimes -\mathrm{i}\sigma_z$ the representation of C_{2z} in the orbital basis $|\boldsymbol{\varphi}, \boldsymbol{k}\rangle$, and D_π is the rotation matrix by π around the z axis). Writing $|\boldsymbol{u}, \bar{\boldsymbol{k}} + \boldsymbol{K}\rangle = \hat{T}^{\dagger}(\boldsymbol{K})|\boldsymbol{u}, \bar{\boldsymbol{k}}\rangle$ where $\hat{T}(\boldsymbol{K}) = \mathrm{diag}(\mathrm{e}^{\mathrm{i}r_A\boldsymbol{K}}, \mathrm{e}^{\mathrm{i}r_A\boldsymbol{K}}, \mathrm{e}^{\mathrm{i}r_B\boldsymbol{K}}, \mathrm{e}^{\mathrm{i}r_B\boldsymbol{K}})$ accounts for the phase factors due to the displacements of the sublattice sites with respect to the origin of the unit cell, we can rewrite $R_2^{\bar{\boldsymbol{k}}} = \langle \boldsymbol{u}, \bar{\boldsymbol{k}}|\hat{T}(D_\pi\bar{\boldsymbol{k}} - \bar{\boldsymbol{k}})\hat{U}(C_{2z})|\boldsymbol{u}, \bar{\boldsymbol{k}}\rangle$ which guarantees that the arbitrary gauge phase factors are removed, and use $|u, D_\pi\bar{\boldsymbol{k}}\rangle = \hat{U}(C_{2z})|u, \bar{\boldsymbol{k}}\rangle.R_2^{\bar{\boldsymbol{k}}\,\dagger}$ in the following. We note that at C_{2z}-invariant momenta, i.e., $D_\pi\bar{\boldsymbol{k}} = \bar{\boldsymbol{k}} + \boldsymbol{K}$ with $\boldsymbol{K}$ a reciprocal lattice vector, we have $[\hat{T}(\boldsymbol{K})\hat{U}(C_{2z}), H(\bar{\boldsymbol{k}})] = 0$ and $R_2^{\bar{\boldsymbol{k}}}$ is diagonal. Since for the fragile phase [$z_2 = 0 \bmod 2$, see Eq. (10), we have $R_2^{X} = (\pm)\mathrm{diag(i, i)}$ and $R_2^{\Gamma} = \mathrm{diag(i, -i)}$ (see Table I), we readily find

$$\{\varphi_1, \varphi_2\} = \{0, \pi\} \bmod 2\pi. \tag{A3}$$

We emphasize that the quantization of the Wilson loop over $\Gamma X\Gamma'$ comes from the repetition of the IRREPs at X (equivalently at Γ). An alternative source of Wilson loop quantization is when both Γ and X are TRIMs in which case the Wilson loop phases are Kramers degenerated at $\{0, 0\}$ or $\{\pi, \pi\}$.

Considering now the base path $l_{\Gamma M\Gamma'}$, we have

$$\mathcal{W}[l_{\Gamma M\Gamma'}] = \mathcal{W}_{\Gamma'\leftarrow M} \cdot \mathcal{W}_{M\leftarrow\Gamma}$$
$$= R_4^{\Gamma} \cdot \mathcal{W}^{-1}_{M\leftarrow\Gamma} \cdot \left(R_4^{M}\right)^{-1} \cdot \mathcal{W}_{M\leftarrow\Gamma}, \tag{A4}$$

where $R_4^{\bar{k}} = \langle \boldsymbol{u}, D_{\pi/2}\bar{\boldsymbol{k}}|\hat{U}(C_{4z})|\boldsymbol{u}, \bar{\boldsymbol{k}}\rangle = \langle \boldsymbol{u}, \bar{\boldsymbol{k}}|\hat{T}(C_{4z}\bar{\boldsymbol{k}} - \bar{\boldsymbol{k}})\hat{U}(C_{4z})|\boldsymbol{u}, \bar{\boldsymbol{k}}\rangle$ is the representation in the basis of Bloch eigenvectors of C_{4z} at $\bar{\boldsymbol{k}}$, with, in the orbital basis $|\boldsymbol{\varphi}, \boldsymbol{k}\rangle$, $\hat{U}(C_{4z}) = \sigma_x \otimes M_4$ where $M_4 = \mathrm{diag}(e^{-i\pi/4}, e^{i\pi/4})$, and we have used $|u, D_{\pi/2}\bar{\boldsymbol{k}}\rangle = \hat{U}(C_{4z})|u, \bar{\boldsymbol{k}}\rangle.R_4^{\bar{k}}.^\dagger$.

Using parallel transported Bloch eigenvectors the Wilson loop becomes diagonal, and we write $\widetilde{\mathcal{W}}_{\mathrm{M}\leftarrow\Gamma} = \mathrm{diag}(e^{i\varphi_a}, e^{i\varphi_b})$. The above expression thus reduces to

$$\widetilde{\mathcal{W}}[l_{\Gamma M\Gamma'}] = \widetilde{R}_4^{\Gamma} \cdot \begin{pmatrix} e^{-i\varphi_a} & 0 \\ 0 & e^{-i\varphi_b} \end{pmatrix} \cdot (\widetilde{R}_4^{M})^{-1} \cdot \begin{pmatrix} e^{i\varphi_a} & 0 \\ 0 & e^{i\varphi_b} \end{pmatrix}. \quad \text{(A5)}$$

Since at C_{4z}-symmetric momenta the parallel transported Bloch eigenvectors are also eigenvectors of the C_{4z} operator, we retrieve irreducible representations $\widetilde{R}_4^{\Gamma} = (\pm)\mathrm{diag}(\omega, \omega^*)$ and $\widetilde{R}_4^{M} = (\pm)\mathrm{diag}(\omega, -\omega^*)$, where the signs depend on the coIRREPs realized at Γ and M (see Table I).

The quantization of the Wilson loop $\widetilde{W}[l_{\Gamma M\Gamma'}]$ depends on the relative spin-z components of the parallel transported Bloch eigenstates at Γ and M, see the discussion in Ref. [38]. Writing $\widetilde{R}_4^{\bar{k}} = \mathrm{diag}(\xi_4^{\bar{k}}(\Gamma_a), \xi_4^{\bar{k}}(\Gamma_b))$, we find

$$\widetilde{\mathcal{W}}[l_{\Gamma M\Gamma'}] = \begin{pmatrix} \xi_4^{\Gamma}(\overline{\Gamma}_a)/\xi_4^{M}(\overline{M}_a) & 0 \\ 0 & \xi_4^{\Gamma}(\overline{\Gamma}_b)/\xi_4^{M}(\overline{M}_b) \end{pmatrix}. \quad \text{(A6)}$$

Assuming the same spin-z component at Γ and M, e.g., with $(\overline{\Gamma}_a, \overline{M}_a, \overline{\Gamma}_b, \overline{M}_b) = (\overline{\Gamma}_5, \overline{M}_8, \overline{\Gamma}_7, \overline{M}_5)$ (see Table I), we find

$$\{\varphi_1', \varphi_2'\} = \{\pi/4, \pi/4\} \bmod 2\pi. \quad \text{(A7)}$$

This matches exactly with the direct numerical evaluation of the Wilson loop shown in Fig. 2(e) in the main text. If instead we assume opposite spin-z components at Γ and M, e.g., with $(\overline{\Gamma}_a, \overline{M}_a, \overline{\Gamma}_b, \overline{M}_b) = (\overline{\Gamma}_5, \overline{M}_5, \overline{\Gamma}_7, \overline{M}_8)$ (see Table I), we find

$$\{\varphi_1', \varphi_2'\} = \{0, \pi\} \bmod 2\pi. \quad \text{(A8)}$$

This later quantization thus corresponds to a system where there is a twisting spin texture from Γ to M, which would require strong Rashba-type spin-orbit coupling.

It thus follows that, in the absence of a twisted spin texture, the Wilson loop phases must wind from $\{\varphi_1, \varphi_2\} = \{0, \pi\}$ to $\{\varphi_1', \varphi_2'\} = \{\pi/4, \pi/4\} \bmod 2\pi$, as we scan over one quarter of the Brillouin zone through the deformation of the base path from $l_{\Gamma X\Gamma'}$ to $l_{\Gamma M\Gamma'}$. There is thus a minimal winding of $(\Delta\varphi_1, \Delta\varphi_2) = (\varphi_1', \varphi_2') - (\varphi_1, \varphi_2) = (+\pi/2, -\pi/2)$. By the action of C_4 symmetry we can recover the whole Brillouin zone for which we predict a minimal winding of the Wilson loop phases of $4(\Delta\varphi_1, \Delta\varphi_2) = (+2\pi, -2\pi)$. This precisely predicts algebraically the numerical evaluation of the Wilson loop over the whole Brillouin zone shown in Fig. 2(d).

We finally conclude that the valence (conduction) subspace of the split $\mathrm{EBR}_{75.5}^{2b}$ is topologically nontrivial as indicated by the finite winding of Wilson loop phases.

APPENDIX B: DERIVATION OF FORMULA EQ. (14) AND EQ. (11)

We give here the algebraic derivation of the Wilson loop over $l_q = \Gamma M' X M \Gamma$ [red loop in Fig. 2(c)] as given in Eq. (11), from which Eq. (14) readily follows by reducing to a single band subspace. We use the algebraic Wilson loop techniques developed in Refs. [13,77] and [6,38,83].

It is convenient to decompose the Wilson loop into the contributions of each segment that connects two successive high-symmetry points, i.e., $\mathcal{W}[l_q] = \mathcal{W}_d\mathcal{W}_c\mathcal{W}_b\mathcal{W}_a$, with

$$\begin{aligned} \mathcal{W}_a &= \langle \boldsymbol{u}, \Gamma|\hat{W}|\boldsymbol{u}, M\rangle, \quad \mathcal{W}_c = \langle \boldsymbol{u}, X|\hat{W}|\boldsymbol{u}, M'\rangle, \\ \mathcal{W}_b &= \langle \boldsymbol{u}, M'|\hat{W}|\boldsymbol{u}, \Gamma\rangle, \quad \mathcal{W}_d = \langle \boldsymbol{u}, M|\hat{W}|\boldsymbol{u}, X\rangle, \end{aligned} \quad \text{(B1)}$$

where $M' = M - \boldsymbol{b}_2$.

We now use symmetries to rewrite $\mathcal{W}_a$ and $\mathcal{W}_d$, as

$$\begin{aligned} \mathcal{W}_a &= \langle \boldsymbol{u}, \Gamma|\hat{W}|\boldsymbol{u}, M\rangle = \langle \boldsymbol{u}, C_{4z}\Gamma|\hat{W}|\boldsymbol{u}, C_{4z}M'\rangle \\ &= R_4^{\Gamma} \cdot \langle \boldsymbol{u}, \Gamma|\hat{U}^\dagger(C_{4z})\hat{W}\hat{U}(C_{4z})|\boldsymbol{u}, M'\rangle \cdot \left(R_4^{M'}\right)^\dagger \\ &= R_4^{\Gamma} \cdot \mathcal{W}_b^{-1} \cdot \left(R_4^{M'}\right)^\dagger, \\ \mathcal{W}_d &= \langle \boldsymbol{u}, M|\hat{W}|\boldsymbol{u}, X\rangle = \langle \boldsymbol{u}, C_{2z}\mathrm{M''}|\hat{W}|\boldsymbol{u}, C_{2z}\mathrm{X'}\rangle \\ &= R_2^{\mathrm{M''}} \cdot \langle \boldsymbol{u}, \mathrm{M''}|\hat{U}^\dagger(C_{2z})\hat{W}\hat{U}(C_{2z})|\boldsymbol{u}, \mathrm{X'}\rangle \cdot \left(R_2^{\mathrm{X'}}\right)^\dagger \\ &= R_2^{\mathrm{M''}} \cdot \langle \boldsymbol{u}, M'|\hat{T}(-\boldsymbol{b}_1)\hat{U}^\dagger(C_{2z})\hat{W}\hat{U}(C_{2z})|\hat{T}^\dagger(-\boldsymbol{b}_1)\boldsymbol{u}, \mathrm{X'}\rangle \cdot \left(R_2^{\mathrm{X'}}\right)^\dagger \\ &= R_2^{\mathrm{M''}} \cdot \mathcal{W}_c^{-1} \cdot \left(R_2^{\mathrm{X'}}\right)^\dagger, \end{aligned} \quad \text{(B2)}$$

where $\mathrm{M''} = M' - \boldsymbol{b}_1$ and $\mathrm{X'} = X - \boldsymbol{b}_1$. We thus have

$$\mathrm{Det}\,\mathcal{W}[l_q] = \mathrm{Det}\left[R_2^{\mathrm{M''}} \cdot \left(R_2^{\mathrm{X'}}\right)^\dagger \cdot R_4^{\Gamma} \cdot \left(R_4^{M'}\right)^\dagger\right]. \quad \text{(B3)}$$

Defining the irreducible representation of the symmetry $(g|\tau_g)$ in the basis of Bloch eigenstates as

$$S_g^{\bar{k}} = e^{-i\,g\bar{\boldsymbol{k}}\cdot\tau_g}R_g^{\bar{k}}, \quad \text{(B4)}$$

and substituting in the above expression, we get

$$\begin{aligned} \mathrm{Det}\,\mathcal{W}[l_q] &= e^{i\,N_{\mathrm{occ}}\,[(M-X)\cdot\tau_{C_{2z}} + (\Gamma-M)\cdot\tau_{C_{4z}}]} \\ &\quad \times \mathrm{Det}\left[S_2^{M} \cdot \left(S_2^{X}\right)^\dagger \cdot S_4^{\Gamma} \cdot \left(S_4^{M}\right)^\dagger\right] \\ &= e^{i\,N_{\mathrm{occ}}\,[(M-X)\cdot\tau_{C_{2z}} + (\Gamma-M)\cdot\tau_{C_{4z}}]} \prod_{i=1}^{N_{\mathrm{occ}}} \frac{\xi_4^{\Gamma}(i)\xi_2^{M}(i)}{\xi_4^{M}(i)\xi_2^{X}(i)}, \end{aligned} \quad \text{(B5)}$$

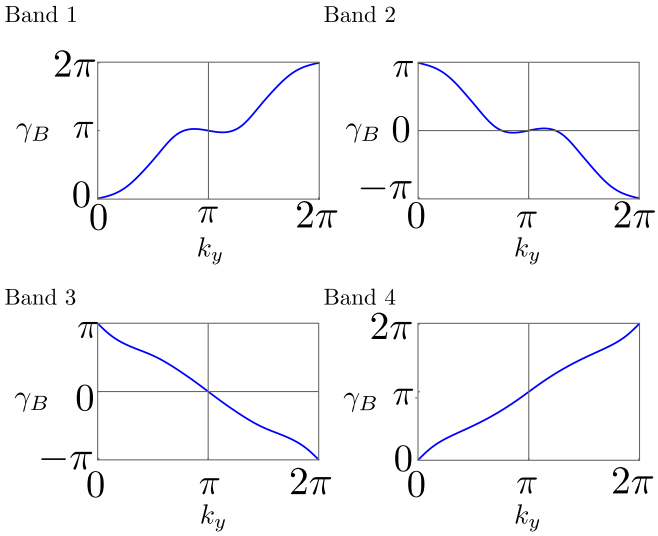

FIG. 12. Berry phase flows for the four split bands of MSG75.1 ($P4$) as obtained from gapping the fragile topological MSG75.5 (P_C4) phase. Bands 1 and 4 have Chern number $\mathcal{C} = +1$. Bands 2 and 3 exhibit Chern number $\mathcal{C} = -1$.

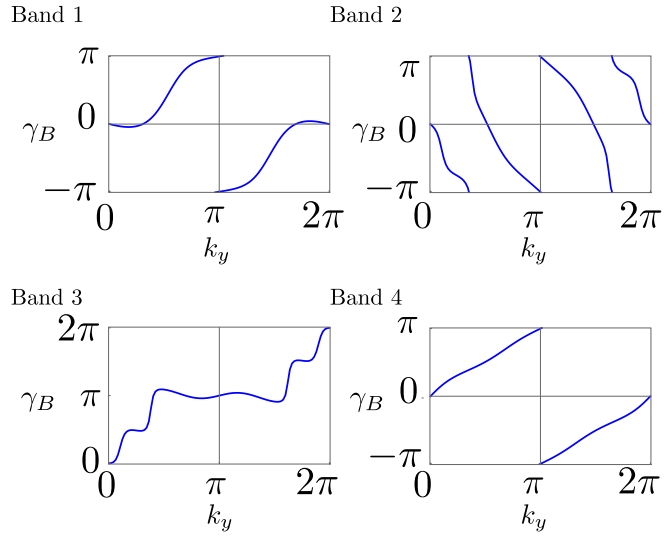

FIG. 13. Berry phase flows for the four split bands of MSG75.1 ($P4$) obtained from the gapping of the stable nodal phase of MSG75.5 (P_C4). Bands 1, 3, and 4 have Chern number $\mathcal{C} = +1$. Bands 2 has has higher Chern number $\mathcal{C} = -3$.

where N_{occ} is the number of occupied bands, and $\xi_g^{\bar{\boldsymbol{k}}}(i)$ is the eigenvalue of the symmetry $(g|\tau_g)$ of the ith band at the high-symmetry momentum $\bar{\boldsymbol{k}}$. For magnetic space groups with symmorphic C_{4z} and C_{2z} symmetries (i.e., $\tau_{C_{4z}} = \tau_{C_{2z}} = 0$) as MSG75.5 (and MSG75.1), it simplifies to

$$\text{Det}\, \mathcal{W}[l_q] = \prod_{i=1}^{N_{\text{occ}}} \frac{\xi_4^{\Gamma}(i)\xi_2^{M}(i)}{\xi_4^{M}(i)\xi_2^{X}(i)}. \tag{B6}$$

APPENDIX C: NUMERICAL COMPUTATION OF BERRY PHASE FLOWS FOR MSG75.1 ($P4$)

We present here the numerical evaluation of the nontriviality of the case MSG75.1 ($P4$), i.e., for the model Eq. (4) with an additional Zeeman coupling. In Fig. 12, we show the numerically obtained Berry phase for the individual bands of the band structure in Fig. 5 obtained for the model of MSG75.1 ($P4$). These evaluations corroborate the analytical results. That is, each band shows a finite Chern number $\mathcal{C}$. While bands 2 and 3 exhibit a value of $\mathcal{C} = 1$, the other two bands have opposite Chern number. Finally, we also show in Fig. 13 the Berry phase of the bands as obtained from gapping the stable nodal topological MSG75.5 (P_C4) band structure of Fig. 3. As described in the main text, the resulting spectrum features a single band (band number two in this case) with Chern number $\mathcal{C} = -3$, whereas the others exhibit a Chern number $\mathcal{C} = 1$.

APPENDIX D: DETAILS ON SYMMETRY INDICATOR ANALYSIS

We here give further detail on the symmetry indicator analysis for some of the MSGs considered.

1. Symmetry indicators for MSG75.5 (P_C4)

MSG75.5 (P_C4) is derived from SG75 by including the operator $(E|\tau)'$ with $\tau = \frac{1}{2}(\mathbf{a}_1 + \mathbf{a}_2)$. We can thus classify the possible band structures for our model by considering the IRREPs of SG75, and pair them appropriately to form coIRREPs of MSG75.5 (P_C4), as described in Ref. [35]. The full compatibility relations [23] and EBRs for SG75 can be found on the Bilbao Crystallographic Server [69]. Using their notation (see also Table I), the compatibility relations for the Γ point are given by

$$\overline{\Gamma}_5 \to \overline{Z}_5, \quad \overline{\Gamma}_6 \to \overline{Z}_6, \quad \overline{\Gamma}_7 \to \overline{Z}_7, \quad \overline{\Gamma}_7 \to \overline{Z}_8. \tag{D1}$$

The compatibility relations between M and A display a similar structure. Finally, the compatibility relations between X and R are

$$\overline{X}_3 \to \overline{R}_3, \quad \overline{X}_4 \to \overline{R}_4. \tag{D2}$$

From the above relations it is evident that it suffices to consider the points Γ, X, and M as the compatibility relations uniquely link IRREPs at these points to all IRREPs at all other high-symmetry points in the 3D BZ [23]. To form the coIRREPs, we consider the additional constraints imposed by the antiunitary symmetries. These can be determined from the Herring rule [57] applied at each high-symmetry point. We only consider spinful IRREPs. At Γ and M (and A and Z), this gives pairing of inequivalent IRREPs. At X (and R), no additional pairing is required. To determine which IRREPs are paired to form the coIRREPs at Γ and M, we pair representations of g with representations of AgA^{-1}, where g is an element of the unitary little group at Γ or M and $A = (E|\tau)'$. The allowed pairings at Γ are $\overline{\Gamma}_5\overline{\Gamma}_7$, $\overline{\Gamma}_6\overline{\Gamma}_8$ and the pairings at M are $\overline{M}_6\overline{M}_7$, $\overline{M}_5\overline{M}_8$.

The magnetic EBRs for the MSG75.5 (P_C4) can be found from the EBRs for SG75 [69]. We note that the vector τ relates WP $1a$ $(0,0)$ and $1b$ $(1/2,1/2)$ in SG75, so the EBRs from these WPs are paired. Similarly, τ maps WP

$2c$ $(0, 1/2)$, $(1/2, 0)$ in SG75 to itself, so we pair EBRs at WP $2c$ directly. We can uniquely determine which EBRs are paired, by realizing that the magnetic EBRs must satisfy the magnetic compatibility relations detailed above. This gives the following magnetic EBRs for MSG75.5 (P_C4) (using the WP labels from SG75):

$$(1a:\ {}^1\overline{E}_1 + 1b:\ {}^2\overline{E}_2) \uparrow G = (\overline{\Gamma}_6\overline{\Gamma}_8, \overline{M}_6\overline{M}_7, 2\overline{X}_3), \quad (1a:\ {}^1\overline{E}_2 + 1b:\ {}^2\overline{E}_1) \uparrow G = (\overline{\Gamma}_5\overline{\Gamma}_7, \overline{M}_5\overline{M}_8, 2\overline{X}_3),$$
$$(1a:\ {}^2\overline{E}_1 + 1b:\ {}^1\overline{E}_2) \uparrow G = (\overline{\Gamma}_6\overline{\Gamma}_8, \overline{M}_5\overline{M}_8, 2\overline{X}_4), \quad (1a:\ {}^2\overline{E}_2 + 1b:\ {}^1\overline{E}_1) \uparrow G = (\overline{\Gamma}_5\overline{\Gamma}_6, \overline{M}_6\overline{M}_7, 2\overline{X}_4),$$
$$(2c:\ {}^1\overline{E} + 2c:\ {}^2\overline{E}) \uparrow G = (\overline{\Gamma}_5\overline{\Gamma}_6\overline{\Gamma}_7\overline{\Gamma}_8, \overline{M}_5\overline{M}_6\overline{M}_7\overline{M}_8, 2\overline{X}_4 2\overline{X}_3).$$

To compute the symmetry indicators, as described in Ref. [35], we compute the Smith normal form of the matrix of EBRs. This gives the indicator group for MSG75.5 (P_C4) as $\mathbb{Z}_2$, in agreement with [35].

From our magnetic EBRs, we see that it is not possible to construct a band structure with an odd number of bands in the $\overline{X}_3$ (or equivalently the $\overline{X}_4$) IRREP from an integer combination of magnetic EBRs. Every other combination consistent with the compatibility relations can be constructed from the magnetic EBRs. Thus, the $\mathbb{Z}_2$ indicator can be conveniently computed as

$$n_{\overline{X}_3} \bmod 2, \tag{D3}$$

in agreement with the expression in the main text.

2. Symmetry indicators for MSG77.18 (P_I4_2)

MSG77.18 (P_I4_2) is formed from SG77, by including the operator $(E|\tau)'$ with $\tau = \frac{1}{2}(\mathbf{a}_1 + \mathbf{a}_2 + \mathbf{a}_3)$. For the C_4 symmetric points (Γ, Z, M, A), the Herring test gives the same result as for 75.5. At X, the Herring test gives that the antiunitary symmetries impose no further degeneracies, whereas at R, the Herring test gives that each IRREP must be doubly degenerate. Additional degeneracies are imposed by the nonsymmorphic symmetry elements of SG77. For the C_4 symmetric points, the nonsymmorphic symmetries constrain that the IRREPs must switch partners when moving through the BZ. This enforces gap closings along the k_z direction, which acts as an obstruction to defining two-band subspaces across the entire BZ, see Figs. 7(a) and 7(c). Thus the minimal connectivity of bands in the BZ is 4. The symmetry indicator group can be computed as before. WP $2c$ $(0, 1/2, z)$, $(0, 1/2, z + 1/2)$ of SG77 goes into WP $2a$ of MSG77.18 (P_I4_2), and the two spinful site-symmetry IRREPs glue together. Similarly, WP $2a$ $(0, 0, z)$, $(0, 0, z + 1/2)$ and $2b$ $(1/2, 1/2, z)$, $(1/2, 1/2, z + 1/2)$ of SG77 go into WP $4b$ of MSG77.18 (P_I4_2), and by checking the compatibility relations, we realize that IRREPs ${}^1\overline{E}$ pairs with ${}^2\overline{E}$ at the different sites. Thus we get three spinful magnetic EBRs, which are given by (using the WP labels from SG77):

$$(2c:\ \overline{E}_1 + 2c:\ \overline{E}_2) \uparrow G = (\overline{\Gamma}_5\overline{\Gamma}_6\overline{\Gamma}_7\overline{\Gamma}_8, \overline{Z}_5\overline{Z}_6\overline{Z}_7\overline{Z}_8, \overline{M}_5\overline{M}_6\overline{M}_7\overline{M}_8, \overline{A}_5\overline{A}_6\overline{A}_7\overline{A}_8, 2\overline{X}_3 2\overline{X}_4, 2\overline{R}_3 2\overline{R}_4),$$
$$(2a:\ \overline{E}_1 + 2b:\ \overline{E}_2) \uparrow G = (\overline{\Gamma}_5\overline{\Gamma}_6\overline{\Gamma}_7\overline{\Gamma}_8, \overline{Z}_5\overline{Z}_6\overline{Z}_7\overline{Z}_8, \overline{M}_5\overline{M}_6\overline{M}_7\overline{M}_8, \overline{A}_5\overline{A}_6\overline{A}_7\overline{A}_8, 4\overline{X}_3, 4\overline{R}_3),$$
$$(2a:\ \overline{E}_2 + 2b:\ \overline{E}_1) \uparrow G = (\overline{\Gamma}_5\overline{\Gamma}_6\overline{\Gamma}_7\overline{\Gamma}_8, \overline{Z}_5\overline{Z}_6\overline{Z}_7\overline{Z}_8, \overline{M}_5\overline{M}_6\overline{M}_7\overline{M}_8, \overline{A}_5\overline{A}_6\overline{A}_7\overline{A}_8, 4\overline{X}_4, 4\overline{R}_4).$$

Using the Smith normal form decomposition as before, we see that there's no nontrivial indicator in this MSG, in agreement with Ref. [35].

3. Symmetry indicator for MSG81.36 ($P_c\bar{4}$)

As a final example, we here compute the symmetry indicators for MSG81.36 ($P_c\bar{4}$), as an example of an MSG with S_4 rotoinversion symmetry. This MSG is generated from SG81 by including the operator $(E|\tau)'$ with $\tau = \frac{1}{2}\mathbf{a}_3$. SG81 is similar to SG75, but the C_4 rotations are combined with inversion. The Herring test gives that the C_2 IRREPs must glue together at the C_2 symmetric points X and R. At the C_4 symmetric points, the Herring test glues together $\overline{\Gamma}_5\overline{\Gamma}_7$ and $\overline{\Gamma}_6\overline{\Gamma}_8$, respectively, and similarly at M. At Z, $\overline{Z}_5\overline{Z}_8$ and $\overline{Z}_6\overline{Z}_7$ glue together respectively, and similarly at A. This assignment satisfies the compatibility relations, so the minimal connectivity of bands in the BZ is 2, and two-band subspaces can be defined throughout the BZ.

To compute the symmetry indicator group, we note that τ connects WP $1a$ $(0, 0, 0)$ and $1b$ $(0, 0, 1/2)$ of SG81 to form magnetic WP $2a$. Similarly, WP $1c$ $(1/2, 1/2, 0)$ and $1d$ $(1/2, 1/2, 1/2)$ of SG81 connect to form magnetic WP $2c$. Some of the nonmaximal WPs of SG81 become maximal WPs for MSG81.36 ($P_c\bar{4}$), e.g., WP $2e$ $(0, 0, z)$, $(0, 0, -z)$ of SG81 goes into maximal magnetic WP $2b$ $(0, 0, 1/4)$, $(0, 0, 3/4)$, and similarly for nonmagnetic WP $2f$ going into magnetic WP $2d$. As the EBRs at these WPs have to satisfy compatibility relations, however, it is straightforward to investigate which site-symmetry IRREPs to pair. This gives the following magnetic EBRs (labelled using the WPs of SG81):

$$(1a:\ {}^1\overline{E}_1 + 1b:\ {}^2\overline{E}_1) \uparrow G = (\overline{\Gamma}_6\overline{\Gamma}_8, \overline{Z}_6\overline{Z}_7, \overline{M}_6\overline{M}_8, \overline{A}_6\overline{A}_7, \overline{X}_3\overline{X}_4, \overline{R}_3\overline{R}_4),$$
$$(1a:\ {}^1\overline{E}_2 + 1b:\ {}^2\overline{E}_2) \uparrow G = (\overline{\Gamma}_5\overline{\Gamma}_7, \overline{Z}_5\overline{Z}_8, \overline{M}_5\overline{M}_7, \overline{A}_5\overline{A}_8, \overline{X}_3\overline{X}_4, \overline{R}_3\overline{R}_4),$$
$$(1a:\ {}^2\overline{E}_1 + 1b:\ {}^1\overline{E}_1) \uparrow G = (\overline{\Gamma}_6\overline{\Gamma}_8, \overline{Z}_5\overline{Z}_8, \overline{M}_6\overline{M}_8, \overline{A}_5\overline{A}_8, \overline{X}_3\overline{X}_4, \overline{R}_3\overline{R}_4),$$
$$(1a:\ {}^2\overline{E}_2 + 1b:\ {}^1\overline{E}_2) \uparrow G = (\overline{\Gamma}_5\overline{\Gamma}_7, \overline{Z}_6\overline{Z}_7, \overline{M}_5\overline{M}_7, \overline{A}_6\overline{A}_7, \overline{X}_3\overline{X}_4, \overline{R}_3\overline{R}_4),$$

$$(1c:\ {}^1\overline{E}_1 + 1d:\ {}^2\overline{E}_1) \uparrow G = (\overline{\Gamma}_6\overline{\Gamma}_8, \overline{Z}_6\overline{Z}_7, \overline{M}_5\overline{M}_7, \overline{A}_5\overline{A}_8, \overline{X}_3\overline{X}_4, \overline{R}_3\overline{R}_4),$$

$$(1c:\ {}^1\overline{E}_2 + 1d:\ {}^2\overline{E}_2) \uparrow G = (\overline{\Gamma}_5\overline{\Gamma}_7, \overline{Z}_5\overline{Z}_8, \overline{M}_6\overline{M}_8, \overline{A}_6\overline{A}_7, \overline{X}_3\overline{X}_4, \overline{R}_3\overline{R}_4),$$

$$(1c:\ {}^2\overline{E}_1 + 1b:\ {}^1\overline{E}_1) \uparrow G = (\overline{\Gamma}_6\overline{\Gamma}_8, \overline{Z}_5\overline{Z}_8, \overline{M}_5\overline{M}_7, \overline{A}_6\overline{A}_7, \overline{X}_3\overline{X}_4, \overline{R}_3\overline{R}_4),$$

$$(1c:\ {}^2\overline{E}_2 + 1d:\ {}^1\overline{E}_2) \uparrow G = (\overline{\Gamma}_5\overline{\Gamma}_7, \overline{Z}_6\overline{Z}_7, \overline{M}_6\overline{M}_8, \overline{A}_5\overline{A}_8, \overline{X}_3\overline{X}_4, \overline{R}_3\overline{R}_4),$$

$$(2e:\ {}^1\overline{E} + 2e:\ {}^2\overline{E}) \uparrow G = (\overline{\Gamma}_5\overline{\Gamma}_6\overline{\Gamma}_7\overline{\Gamma}_8, \overline{Z}_5\overline{Z}_6\overline{Z}_7\overline{Z}_8, \overline{M}_5\overline{M}_6\overline{M}_7\overline{M}_8, \overline{A}_5\overline{A}_6\overline{A}_7\overline{A}_8, 2\overline{X}_32\overline{X}_4, 2\overline{R}_32\overline{R}_4),$$

$$(2f:\ {}^1\overline{E} + 2f:\ {}^2\overline{E}) \uparrow G = (\overline{\Gamma}_5\overline{\Gamma}_6\overline{\Gamma}_7\overline{\Gamma}_8, \overline{Z}_5\overline{Z}_6\overline{Z}_7\overline{Z}_8, \overline{M}_5\overline{M}_6\overline{M}_7\overline{M}_8, \overline{A}_5\overline{A}_6\overline{A}_7\overline{A}_8, 2\overline{X}_32\overline{X}_4, 2\overline{R}_32\overline{R}_4).$$

Computing the Smith normal form gives a single $\mathbb{Z}_2$ factor. Inspecting the solution space, we see that the corresponding indicator is given by whether the IRREPs at the C_4 invariant points contain an odd or an even number of representations with subscript 5 (or any other subscript). Thus an explicit expression for the symmetry indicator is

$$z_2' = n_{\overline{\Gamma}_5} + n_{\overline{Z}_5} + n_{\overline{M}_5} + n_{\overline{A}_5} \bmod 2. \tag{D4}$$

It has been shown in [36] for MSG81.33 ($P\bar{4}$) that this symmetry indicator relates to a 3D axion topological insulating phase.

We finally note that our results in this Appendix agree with general expressions for magnetic EBRs, compatibility relations and symmetry indicators in Ref. [36], which we became aware of during the finalizing stages of this manuscript.

[1] X.-L. Qi and S.-C. Zhang, Topological insulators and superconductors, Rev. Mod. Phys. **83**, 1057 (2011).

[2] M. Z. Hasan and C. L. Kane, *Colloquium:* Topological insulators, Rev. Mod. Phys. **82**, 3045 (2010).

[3] R.-J. Slager, A. Mesaros, V. Juričić, and J. Zaanen, The space group classification of topological band-insulators, Nat. Phys. **9**, 98 (2012).

[4] L. Fu, Topological Crystalline Insulators, Phys. Rev. Lett. **106**, 106802 (2011).

[5] R.-J. Slager, The translational side of topological band insulators, J. Phys. Chem. Solids **128**, 24 (2019), spin-Orbit Coupled Materials.

[6] A. Bouhon and A. M. Black-Schaffer, Global band topology of simple and double dirac-point semimetals, Phys. Rev. B **95**, 241101(R) (2017).

[7] T. Bzdušek, QuanSheng Wu, A. Rüegg, M. Sigrist, and A. A. Soluyanov, Nodal-chain metals, Nature (London) **538**, 75 (2016).

[8] J. Höller and A. Alexandradinata, Topological bloch oscillations, Phys. Rev. B **98**, 024310 (2018).

[9] B.-J. Yang and N. Nagaosa, Classification of stable three-dimensional dirac semimetals with nontrivial topology, Nat. Commun. **5**, 4898 (2014).

[10] M. Nakagawa, R.-J. Slager, S. Higashikawa, and T. Oka, Wannier representation of floquet topological states, Phys. Rev. B **101**, 075108 (2020).

[11] F. N. Ünal, A. Eckardt, and R.-J. Slager, Hopf characterization of two-dimensional floquet topological insulators, Phys. Rev. Research **1**, 022003(R) (2019).

[12] K. Shiozaki, M. Sato, and K. Gomi, Topological crystalline materials: General formulation, module structure, and wallpaper groups, Phys. Rev. B **95**, 235425 (2017).

[13] C. Fang, M. J. Gilbert, and B. A. Bernevig, Bulk topological invariants in noninteracting point group symmetric insulators, Phys. Rev. B **86**, 115112 (2012).

[14] D. S. Borgnia, A. J. Kruchkov, and R.-J. Slager, Non-Hermitian Boundary Modes and Topology, Phys. Rev. Lett. **124**, 056802 (2020).

[15] M. Taherinejad, K. F. Garrity, and D. Vanderbilt, Wannier center sheets in topological insulators, Phys. Rev. B **89**, 115102 (2014).

[16] N. Marzari and D. Vanderbilt, Maximally localized generalized wannier functions for composite energy bands, Phys. Rev. B **56**, 12847 (1997).

[17] V. Juričić, A. Mesaros, R.-J. Slager, and J. Zaanen, Universal Probes of Two-Dimensional Topological Insulators: Dislocation and π flux, Phys. Rev. Lett. **108**, 106403 (2012).

[18] M. S. Scheurer and R.-J. Slager, Unsupervised Machine Learning and Band Topology, Phys. Rev. Lett. **124**, 226401 (2020).

[19] A. A. Soluyanov and D. Vanderbilt, Wannier representation of $\mathbb{z}_2$ topological insulators, Phys. Rev. B **83**, 035108 (2011).

[20] R.-J. Slager, L. Rademaker, J. Zaanen, and L. Balents, Impurity-bound states and green's function zeros as local signatures of topology, Phys. Rev. B **92**, 085126 (2015).

[21] A. Mesaros, R.-J. Slager, J. Zaanen, and V. Juricic, Zero-energy states bound to a magnetic π-flux vortex in a two-dimensional topological insulator, Nucl. Phys. B **867**, 977 (2013).

[22] J.-W. Rhim, J. H. Bardarson, and R.-J. Slager, Unified bulk-boundary correspondence for band insulators, Phys. Rev. B **97**, 115143 (2018).

[23] J. Kruthoff, J. de Boer, J. van Wezel, C. L. Kane, and R.-J. Slager, Topological Classification of Crystalline Insulators Through Band Structure Combinatorics, Phys. Rev. X **7**, 041069 (2017).

[24] H. C. Po, A. Vishwanath, and H. Watanabe, Symmetry-based indicators of band topology in the 230 space groups, Nat. Commun. **8**, 50 (2017).

[25] B. Bradlyn, L. Elcoro, J. Cano, M. G. Vergniory, Z. Wang, C. Felser, M. I. Aroyo, and B. A. Bernevig, Topological quantum chemistry, Nature (London) **547**, 298 (2017).

[26] F. D. M. Haldane, Model for a Quantum Hall Effect without Landau Levels: Condensed-Matter Realization of the Parity Anomaly, Phys. Rev. Lett. **61**, 2015 (1988).

[27] N. Hyun Jo, L.-L. Wang, R.-J. Slager, J. Yan, Y. Wu, K. Lee, B. Schrunk, A. Vishwanath, and A. Kaminski, Intrinsic axion insulating behavior in antiferromagnetic $MnBi_6Te_{10}$, Phys. Rev. B **102**, 045130 (2020).

[28] X.-L. Qi, T. L. Hughes, and S.-C. Zhang, Topological field theory of time-reversal invariant insulators, Phys. Rev. B **78**, 195424 (2008).

[29] N. Varnava and D. Vanderbilt, Surfaces of axion insulators, Phys. Rev. B **98**, 245117 (2018).

[30] B. J. Wieder and B. A. Bernevig, The axion insulator as a pump of fragile topology, arXiv:1810.02373.

[31] C. Liu, Y. Wang, H. Li, Y. Wu, Y. Li, J. Li, Ke He, Y. Xu, J. Zhang, and Y. Wang, Robust axion insulator and chern insulator phases in a two-dimensional antiferromagnetic topological insulator, Nat. Mater. **19**, 522 (2020).

[32] R. S. K. Mong, A. M. Essin, and J. E. Moore, Antiferromagnetic topological insulators, Phys. Rev. B **81**, 245209 (2010).

[33] M. M. Otrokov, I. I. Klimovskikh, H. Bentmann, D. Estyunin, A. Zeugner, Z. S. Aliev, S. Gaß, A. U. B. Wolter, A. V. Koroleva, A. M. Shikin, M. Blanco-Rey, M. Hoffmann, I. P. Rusinov, A. Yu. Vyazovskaya, S. V. Eremeev, Yu. M. Koroteev, V. M. Kuznetsov, F. Freyse, J. Sánchez-Barriga, I. R. Amiraslanov, M. B. Babanly, N. T. Mamedov, N. A. Abdullayev, V. N. Zverev, A. Alfonsov, V. Kataev, B. Büchner, E. F. Schwier, S. Kumar, A. Kimura, L. Petaccia, G. Di Santo, R. C. Vidal, S. Schatz, K. Kißner, M. Ünzelmann, C. H. Min, Simon Moser, T. R. F. Peixoto, F. Reinert, A. Ernst, P. M. Echenique, A. Isaeva, and E. V. Chulkov, Prediction and observation of an antiferromagnetic topological insulator, Nature (London) **576**, 416 (2019).

[34] R.-X. Zhang and C.-X. Liu, Topological magnetic crystalline insulators and corepresentation theory, Phys. Rev. B **91**, 115317 (2015).

[35] H. Watanabe, H. C. Po, and A. Vishwanath, Structure and topology of band structures in the 1651 magnetic space groups, Sci. Adv. **4**, eaat8685 (2018).

[36] L. Elcoro, B. J. Wieder, Z. Song, Y. Xu, B. Bradlyn, and B. A. Bernevig, Magnetic topological quantum chemistry, arXiv:2010.00598 [cond-mat.mes-hall].

[37] H. C. Po, H. Watanabe, and A. Vishwanath, Fragile Topology and Wannier Obstructions, Phys. Rev. Lett. **121**, 126402 (2018).

[38] A. Bouhon, A. M. Black-Schaffer, and R.-J. Slager, Wilson loop approach to fragile topology of split elementary band representations and topological crystalline insulators with time-reversal symmetry, Phys. Rev. B **100**, 195135 (2019).

[39] V. Peri, Z.-D. Song, M. Serra-Garcia, P. Engeler, R. Queiroz, X. Huang, W. Deng, Z. Liu, B. A. Bernevig, and S. D. Huber, Experimental characterization of fragile topology in an acoustic metamaterial, Science **367**, 797 (2020).

[40] Z. Song, L. Elcoro, N. Regnault, and B. A. Bernevig, Fragile Phases as Affine Monoids: Full Classification and Material Examples, Phys. Rev. X **10**, 031001 (2020).

[41] Y. Hwang, J. Ahn, and B.-J. Yang, Fragile topology protected by inversion symmetry: Diagnosis, bulk-boundary correspondence, and wilson loop, Phys. Rev. B **100**, 205126 (2019).

[42] C. Fang and L. Fu, New classes of three-dimensional topological crystalline insulators: Nonsymmorphic and magnetic, Phys. Rev. B **91**, 161105(R) (2015).

[43] C. Fang, Y. Chen, H.-Y. Kee, and L. Fu, Topological nodal line semimetals with and without spin-orbital coupling, Phys. Rev. B **92**, 081201(R) (2015).

[44] J. Ahn and B.-J. Yang, Unconventional Topological Phase Transition in Two-Dimensional Systems with Space-Time Inversion Symmetry, Phys. Rev. Lett. **118**, 156401 (2017).

[45] Y. X. Zhao and Y. Lu, PT-Symmetric Real Dirac Fermions and Semimetals, Phys. Rev. Lett. **118**, 056401 (2017).

[46] T. Bzdušek and M. Sigrist, Robust doubly charged nodal lines and nodal surfaces in centrosymmetric systems, Phys. Rev. B **96**, 155105 (2017).

[47] J. Ahn, D. Kim, Y. Kim, and B.-J. Yang, Band Topology and Linking Structure of Nodal Line Semimetals with Z_2 Monopole Charges, Phys. Rev. Lett. **121**, 106403 (2018).

[48] J. Ahn, S. Park, and B.-J. Yang, Failure of Nielsen-Ninomiya Theorem and Fragile Topology in Two-Dimensional Systems with Space-Time Inversion Symmetry: Application to Twisted Bilayer Graphene at Magic Angle, Phys. Rev. X **9**, 021013 (2019).

[49] A. Bouhon, T. Bzdušek, and R.-J. Slager, Geometric approach to fragile topology beyond symmetry indicators, Phys. Rev. B **102**, 115135 (2020).

[50] F. N. Ünal, A. Bouhon, and R.-J. Slager, Topological Euler Class as a Dynamical Observable in Optical Lattices, Phys. Rev. Lett. **125**, 053601 (2020).

[51] QuanSheng Wu, A. A. Soluyanov, and T. Bzdušek, Non-abelian band topology in noninteracting metals, Science **365**, 1273 (2019).

[52] A. Bouhon, QuanSheng Wu, R.-J. Slager, H. Weng, O. V. Yazyev, and T. Bzdušek, Non-abelian reciprocal braiding of weyl points and its manifestation in zrte, Nat. Phys. **16**, 1137 (2020).

[53] Z. Song, Z. Wang, W. Shi, G. Li, C. Fang, and B. A. Bernevig, All Magic Angles in Twisted Bilayer Graphene are Topological, Phys. Rev. Lett. **123**, 036401 (2019).

[54] H. C. Po, L. Zou, T. Senthil, and A. Vishwanath, Faithful tight-binding models and fragile topology of magic-angle bilayer graphene, Phys. Rev. B **99**, 195455 (2019).

[55] S. M. Young and B. J. Wieder, Filling-Enforced Magnetic Dirac Semimetals in Two Dimensions, Phys. Rev. Lett. **118**, 186401 (2017).

[56] G. F. Lange, A. Bouhon, and R.-J. Slager, Subdimensional topologies, indicators, and higher order boundary effects, Phys. Rev. B **103**, 195145 (2021).

[57] C. J. Bradley and A. P. Cracknell, *The Mathematical Theory of Symmetry in Solids* (Oxford University Press, Oxford, 1972).

[58] D. B. Litvin, *1-, 2- and 3-Dimensional Magnetic Subperiodic Groups and Magnetic Space Groups* (International Union of Crystallography, 1972).

[59] J. Kübler, *Theory of Itinerant Electron Magnetism* (Oxford Science Publications, 2009).

[60] B. Skubic, J. Hellsvik, L. Nordström, and O. Eriksson, A method for atomistic spin dynamics simulations: Implementation and examples. J. Phys.: Condens. Matter **20**, 315203 (2008).

[61] A. Bergman, L. Bergqvist, O. Eriksson, and J. Hellsvik, *Atomistic Spin Dynamics: Foundations and Applications* (Oxford University Press, 2017).

[62] J. L. Alonso, L.A. Fernández, F. Guinea, V. Laliena, and V. Martín-Mayor, Hybrid monte carlo algorithm for the double exchange model, Nucl. Phys. B **596**, 587 (2001).

[63] R. M. Geilhufe, F. Guinea, and V. Juričić, Hund nodal line semimetals: The case of a twisted magnetic phase in the double-exchange model, Phys. Rev. B **99**, 020404(R) (2019).

[64] J. Zak, Symmetry Specification of Bands in Solids, Phys. Rev. Lett. **45**, 1025 (1980).

[65] J. Zak, Band representations and symmetry types of bands in solids, Phys. Rev. B **23**, 2824 (1981).

[66] L. Michel and J. Zak, Connectivity of energy bands in crystals, Phys. Rev. B **59**, 5998 (1999).

[67] K. Shiozaki and M. Sato, Topology of crystalline insulators and superconductors, Phys. Rev. B **90**, 165114 (2014).

[68] K. Shiozaki, M. Sato, and K. Gomi, Topology of nonsymmorphic crystalline insulators and superconductors, Phys. Rev. B **93**, 195413 (2016).

[69] M. I. Aroyo, A. Kirov, C. Capillas, J. M. Perez-Mato, and H. Wondratschek, Bilbao Crystallographic Server. II. Representations of crystallographic point groups and space groups, Acta Cryst. A **62**, 115 (2006).

[70] R. Evarestov and V. P. Smirnov, *Site Symmetry in Crystals* (Springer-Verlag Berlin Heidelberg, 1997).

[71] A. Hatcher, *Vector Bundles and K-Theory* (unpublished).

[72] J. Zak, Berry's Phase for Energy Bands in Solids, Phys. Rev. Lett. **62**, 2747 (1989).

[73] B. Bradlyn, Z. Wang, J. Cano, and B. A. Bernevig, Disconnected elementary band representations, fragile topology, and wilson loops as topological indices: An example on the triangular lattice, Phys. Rev. B **99**, 045140 (2019).

[74] S. H. Kooi, G. van Miert, and C. Ortix, Classification of crystalline insulators without symmetry indicators: Atomic and fragile topological phases in twofold rotation symmetric systems, Phys. Rev. B **100**, 115160 (2019).

[75] B. Lian, F. Xie, and B. A. Bernevig, Landau level of fragile topology, Phys. Rev. B **102**, 041402(R) (2020).

[76] *International Tables for Crystallography. Volume A, Space-Group Symmetry*, online ed. edited by T. Hahn (2006).

[77] Z. Wang, A. Alexandradinata, R. J. Cava, and B. A. Bernevig, Hourglass fermions, Nature (London) **532**, 189 (2016).

[78] C. Fang, M. J. Gilbert, and B. A. Bernevig, Topological insulators with commensurate antiferromagnetism, Phys. Rev. B **88**, 085406 (2013).

[79] J. Ahn and B.-J. Yang, Symmetry representation approach to topological invariants in $C_{2z}t$-symmetric systems, Phys. Rev. B **99**, 235125 (2019).

[80] E. Khalaf, H. C. Po, A. Vishwanath, and H. Watanabe, Symmetry Indicators and Anomalous Surface States of Topological Crystalline Insulators, Phys. Rev. X **8**, 031070 (2018).

[81] A. M. Essin, J. E. Moore, and D. Vanderbilt, Magnetoelectric Polarizability and Axion Electrodynamics in Crystalline Insulators, Phys. Rev. Lett. **102**, 146805 (2009).

[82] V. Mathai and G. C. Thiang, Global topology of weyl semimetals and fermi arcs, J. Phys. A: Math. Theor. **50**, 11LT01 (2017).

[83] A. Bouhon and A. M. Black-Schaffer, Bulk topology of line-nodal structures protected by space group symmetries in class AI, arXiv:1710.04871 [cond-mat.mtrl-sci].

[84] E. Kiritsis, A topological investigation of the Quantum Adiabatic Phase, Commun. Math. Phys. **111**, 417 (1987).

[85] M. Lin and T. L. Hughes, Topological quadrupolar semimetals, Phys. Rev. B **98**, 241103(R) (2018).

[86] Z. Wang, B. J. Wieder, J. Li, B. Yan, and B. A. Bernevig, Higher-Order Topology, Monopole Nodal Lines, and the Origin of Large Fermi arcs in Transition Metal Dichalcogenides xte_2 ($x = $ Mo, W), Phys. Rev. Lett. **123**, 186401 (2019).

[87] B. J. Wieder, Z. Wang, J. Cano, Xi Dai, L. M. Schoop, B. Bradlyn, and B. A. Bernevig, Strong and fragile topological dirac semimetals with higher-order fermi arcs, Nat. Commun. **11**, 627 (2020).

[88] S. S. Tsirkin, I. Souza, and D. Vanderbilt, Composite weyl nodes stabilized by screw symmetry with and without time-reversal invariance, Phys. Rev. B **96**, 045102 (2017).

[89] T. L. Hughes, E. Prodan, and B. A. Bernevig, Inversion-symmetric topological insulators, Phys. Rev. B **83**, 245132 (2011).

[90] A. Alexandradinata, Xi Dai, and B. A. Bernevig, Wilson-loop characterization of inversion-symmetric topological insulators, Phys. Rev. B **89**, 155114 (2014).

[91] A. Alexandradinata and B. A. Bernevig, Berry-phase description of topological crystalline insulators, Phys. Rev. B **93**, 205104 (2016).

[92] R. González-Hernández, E. Tuiran, and B. Uribe, Chiralities of nodal points along high symmetry lines with screw rotation symmetry, arXiv:2102.09970 [cond-mat.mtrl-sci].

[93] H. B. Nielsen and M. Ninomiya, A no-go theorem for regularizing chiral fermions, Phys. Lett. B **105**, 219 (1981).

[94] A. Alexandradinata, Z. Wang, and B. A. Bernevig, Topological Insulators from Group Cohomology, Phys. Rev. X **6**, 021008 (2016).

[95] C. Dryzun and D. Avnir, On the abundance of chiral crystals, Chem. Commun. **48**, 5874 (2012).

[96] B. Bradlyn, J. Cano, Z. Wang, M. G. Vergniory, C. Felser, R. J. Cava, and B. A. Bernevig, Beyond dirac and weyl fermions: Unconventional quasiparticles in conventional crystals, Science **353**, aaf5037 (2016).

[97] G. Chang, S.-Y. Xu, B. J. Wieder, D. S. Sanchez, S.-M. Huang, I. Belopolski, T.-R. Chang, S. Zhang, A. Bansil, H. Lin, and M. Z. Hasan, Unconventional Chiral Fermions and Large Topological Fermi Arcs in Rhsi, Phys. Rev. Lett. **119**, 206401 (2017).

[98] P. Tang, Q. Zhou, and S.-C. Zhang, Multiple Types of Topological Fermions in Transition Metal Silicides, Phys. Rev. Lett. **119**, 206402 (2017).

[99] G. Chang, B. J. Wieder, F. Schindler, D. S. Sanchez, I. Belopolski, S.-M. Huang, B. Singh, Di Wu, T.-R. Chang, T. Neupert, S.-Y. Xu, H. Lin, and M. Z. Hasan, Topological quantum properties of chiral crystals, Nat. Mater. **17**, 978 (2018).

[100] T. Zhang, R. Takahashi, C. Fang, and S. Murakami, Twofold quadruple weyl nodes in chiral cubic crystals, Phys. Rev. B **102**, 125148 (2020).

[101] B. Peng, Yi Jiang, Z. Fang, H. Weng, and C. Fang, Topological classification and diagnosis in magnetically ordered electronic materials, arXiv:2102.12645 [cond-mat.mes-hall].